



Sensitivity study on the main tidal constituents of the Gulf of Tonkin by using the frequency-domain tidal solver in T-UGOm.

5

Violaine Piton^{1,2}, Marine Herrmann^{1,2}, Florent Lyard¹, Patrick Marsaleix⁽³⁾, Thomas Duhaut³, Damien Allain¹, Sylvain Ouillon^{1,2}

⁽¹⁾ LEGOS, IRD, UMR556 IRD/CNES/CNRS/University of Toulouse, 31400 Toulouse,
10 France

⁽²⁾ LOTUS Laboratory, University of Science and Technology of Hanoi (USTH), Vietnam Academy of Science and Technology (VAST), 18 Hoang Quoc Viet, Cau Giay, Hanoi, Vietnam

⁽³⁾ LA, CNRS, University of Toulouse, 31400 Toulouse, France

15 *Correspondence to:* Violaine Piton violaine.piton@legos.obs-mip.fr

20

25

30



Abstract

Tidal dynamics consequences on hydro-sedimentary processes are a recurrent issue in estuarine and coastal processes studies and accurate tidal solutions are a prerequisite for modelling sediment transport, especially in macro-tidal regions. The motivation for the study presented in this publication is to implement and optimize the model configuration that will satisfy this prerequisite in the frame of a larger objective to study the sediment dynamics and fate in the Red River delta to the Gulf of Tonkin from a numerical hydrodynamical-sediment coupled model. Therefore we focus on the main tidal constituents to conduct sensitivity experiments on the bathymetry and bottom friction parameterization. The frequency-domain solver available in the hydrodynamic unstructured grid model T-UGOm has been used to reduce the computational cost and allow for wider parameter explorations. Tidal solutions obtained from the optimal configuration were evaluated from tide measurements derived from satellite altimetry and show a strong improvement (compared to pre-existing tidal atlases) due to an improved bathymetry dataset and fine friction parameters adjustment. However, our experiments seem to indicate that the solution error budget is still dominated by bathymetry errors, which is the most common limitation for accurate tidal modelling.

50

55

60



65 1. Introduction

The tide impacts on open seas and coastal seas are nowadays largely studied as they influence the oceanic circulation as well as the sediment transport and the ecosystems biogeochemical activity. For instance, Guarnieri et al. (2013) found that tides can influence the circulation by modification of the horizontal advection and can impact on the mixing. According to
70 Gonzalez-Pola et al. (2012) and Wang et al. (2013), tides can also generate strong tidal residual flows by non-linear interactions with the topography. In the South China Sea (SCS), their dissipation can affect the vertical distribution of current and temperature, which in turn might play a role in blooms of the biological communities (Nugroho et al., 2018). The inclusion of tides and tidal forcings in circulation models is therefore not only critical for the
75 representation and study of tides, but also for simulating the circulation and the mixing through different processes: bottom friction modulation by tidal currents, mixing enhanced by vertical tidal currents shear and mixing induced by internal tides, and non-linear interactions between tidal currents and the general circulation (Carter and Merrifield, 2007; Herzfeld, 2009; Guarnieri et al., 2013). Including these mechanisms in circulation models has improved
80 the representation of the seasonal variability of stratifications cycles compared to models without tides (Holt et al., 2017, Maraldi et al, 2013).

At a smaller scale, the effects of tidal currents on the salt and momentum balances in estuaries were first recognized by Pritchard (1954, 1956). Since then, tides are known to play a key role in estuarine dynamics. Affecting mixing, influencing a stronger or weaker
85 stratification depending on the sea water intrusion, and determining the characteristic of the water masses that can interact with the shelf circulation, tides influence is often the main driver of the estuarine dynamics. Amongst others, tidal asymmetry and density gradients are responsible for the presence of estuarine turbidity maximum (mass of highly concentrated suspended sediments, Allen et al., 1980). Slack waters are found to favor sedimentation and
90 deposition, while flood and ebb tend to enhance erosion and resuspension within the estuary, and the tidal asymmetry induce a tidal pumping (i.e. spring tides are more energetic than neap tides). Understanding the dynamics of these turbidity maxima is crucial for harbours and coastal maritime traffic managements as they are often related to high siltation rates,



necessitating regular dredging by local authorities (Owens et al., 2005; Vinh et al., 2018).

95 These zones of accumulation of suspended sediments are also important for the ecology of coastal areas as sediments can carry pollutants that endanger water quality (Eyre and McConchie, 1993). The ability to understand and predict the formation of these zones related to tide cycles is therefore crucial for coastal and local activities.

100 The Gulf of Tonkin (from hereafter GoT) covers an area of 115 000 km² from about 16°10'-21°30'N and 105°30'-111°E. This crescent-shape semi-enclosed basin, also referred as Vịnh Bắc Bộ in Vietnam or as Beibu Gulf in China, is 270 km wide and 500 km long and lies in between China to the North and East, and Vietnam to the West. It is characterized by shallow waters as deep as 90m and is open to the South China Sea (SCS) through the South of the

105 Gulf and to the East through the narrow Hainan Strait (Fig. 1a). This latter, also known as Quiongzhou Strait, is on average 30km wide and 50m deep and separates the Hainan Island from the Zhanjiang Peninsula (mainland China). The bottom topography in the GoT and around Hainan Island is rather complex, constantly changing, especially along the coastlines, and partly unknown. Furthermore, the Ha Long Bay area counts about 2000 islets, also

110 known as notches, sometimes no bigger than a few hundreds square meters.

The GoT is subjected to the South-East Asian sub-tropical monsoon climate (Wyrтки 1961), therefore largely influenced by seasonal water discharges from the Red River (Vietnam) and by many smaller rivers such as the Qinjiang, Nanliu and the Yingzai Rivers (China). The Red River, which brings in average 3500m³/s (Dang et al., 2010) of water along 150km of

115 coastlines, was ranked as the ninth river in the world in terms of sediment discharge in the 1970s with 145-160 Mt/year (Milliman and Meade, 1983). Its sediment supply was drastically reduced since then to around 40 Mt/year of sediments (Le et al., 2007; Vinh et al., 2014). The Red River area accounts for the most populated region of the GoT, with an estimated population of 21.13 millions in 2016, corresponding to an average population

120 density of 994 inhabitants/km² (from the Statistical Yearbook of Vietnam, 2017). This region is also a key to the economy of Vietnam, with Ha Long Bay (a UNESCO world heritage site) for its particular touristic value, and with the Hai Phong ports system, connecting the North of the country to the world market. This latter is the second biggest harbour of Vietnam with a particular fast-growing rate in terms of volume of cargos passing through the port, of about

125 4.5x10⁶ to 36.3x10⁶ tons from 1995 to 2016, respectively (Statistical Yearbook of Vietnam,



2017). However, the harbour of Hai Phong is currently affected by an increasing siltation due to tidal pumping, related to changes in water regulation by dams since the late 80's. Such phenomenon forces a dredging effort more and more important each year, with 6.6 million US \$ spent on dredging activity in 2013 (Lefebvre et al. 2012, Vietnam maritime
130 administration, 2017). In this particular case, fine scale tidal modeling is of great interest for harbour management and risks prevision.

The tides in the SCS and in the GoT have been extensively studied since the 1940s (Nguyen, 1969; Ye and Robinson, 1983; Yu, 1984; Fang, 1986). Skewing through the literature, a lot of
135 discrepancies exist in the cotidal charts before the 1980s, especially over the shelf areas. With the development of numerical models, the discrepancies have been significantly reduced by improving the accuracy of tides and tidal currents prediction.

Wyrcki (1961) was the first to identify the main tidal constituents in the SCS (O_1 , K_1 , M_2 , S_2) and Ye and Robinson (1983), the first to successfully simulate the tides in the area. Until
140 recently, only few numerical studies have focused on the GoT (Fang et al., 1999; Manh and Yanaki, 2000; van Maren et al., 2004) and on the Hainan Strait (Chen et al. 2009). By using, for the first time, a high resolution model (ROMS at $1/25^\circ$) and a combination of all available data, Minh et al. (2014) gave an overview of the dominant physical processes that characterize the tidal dynamics of the GoT, by exploring its resonance spectrum. This study
145 improved the existing state of the art in numerically reproducing the tides of the GoT, however it also showed the limitations of using a 3D model in representing the tidal spectrum. Indeed, large discrepancies between the model and observations especially for the M_2 harmonics and for the phase of S_2 were found. The authors explained those discrepancies by the lack of resolution in the coastal areas due to limitations implied by the use of a regular
150 grid and a poorly resolved bathymetric dataset.

The SCS and the GoT are one of the few regions in the world where diurnal tides dominate the semidiurnal tides (Fang, 1986). The tidal form factor (F), or amplitude ratio, defined by the ratio of the amplitude of the two main semi-diurnal and diurnal constituents, provides a
155 quantitative measure of the general characteristics of the tidal oscillations at a specific location. The following values of F are calculated using tidal amplitudes from FES2014b_synthesis (product described in section 2.2.3). At the entrance of the GoT and at



the Hainan strait, the tides are defined as mixed primarily diurnal with F varying from 1.5 and 2.2 depending on the given locations. At the Red River Delta, F is around 15, attesting of a
160 diurnal regime. Indeed, the major branch of energy flux entering the basin from the southwest is weak for the semi-diurnal tides and strong for the diurnal ones. A second branch of energy (also diurnal tidal waves) enters the GoT through the Hainan Strait (Ding et al., 2013).

In coastal seas and bays, tides are primarily driven by the open ocean tide at the mouth of the
165 bay. By resonance of a constructive interference between the incoming tide and a component reflected from the coast, large tide amplitude can be generated. In the GoT case, tidal waves enter the basin from the adjacent SCS and due to the basin geometry, O_1 and K_1 resonate (Fang et al., 1999). Their amplitudes reach 90 and 80 cm respectively. The Coriolis force deflects to the right the incoming waves and push them against the northern enclosure of the
170 basin. Once the waves are reflected, they propagate southward until they slowly dissipate by friction. Fang (1999) found that the amplitude of the tide gradually decreases from 4 to 2 m North to South during spring tide. The amplitude of O_1 in the GoT is larger than K_1 because of a larger resonance effect, even though its amplitude in the SCS is smaller than K_1 (Minh et al., 2014). The largest semidiurnal waves of the GoT are M_2 and S_2 . They both appear as a
175 degenerated amphidrome with smallest amplitudes near the Red River delta in the northwestern head of the Gulf (between 5 to 15 cm for M_2 and below 5 cm for S_2) (Hu et al., 2001). Given those values of amplitude, Van Maren et al. (2004) defined the tidal regime in the GoT as mesotidal, and locally even macrotidal, even though diurnal tidal regimes are usually mainly microtidal.

180

Our objectives in this paper are to propose a robust and simple approach that allows to improve the tidal representation in the Gulf of Tonkin and to complement the previous studies in tidal modeling in the area. This article represents the first step in a more comprehensive modeling study aiming at representing the transport and the fate of sediments
185 from the Red River to the Gulf.

As evidenced by Fontes et al. (2008) and Le Bars et al. (2010), local tidal simulations are mainly affected by the bathymetry and the bottom stress parametrization. These latter often lack of details in remote coastal regions and/or in poorly sampled regions. It is particularly
190 the case for the GoT. By its location at the boundary between China and Vietnam and by its



intense maritime transport activity, the region is extremely difficult to sample, in particular in the highly protected region of Ha Long Bay, in the strait of Hainan and in the nearshore/coastal areas. In situ data and soundings are consequently rare and yet extremely valuable. The precise goal of the present study is therefore to build an improved bathymetry and coastline database over the GoT and to define the best configuration for bottom stress parameterization in this region, evaluating the impact of those parameters on the tidal representation in the GoT. The resulting optimized configuration will then be used for future numerical studies of ocean dynamics and sediment transport in the region. For that, we first worked on the improvement of the general and global bathymetric datasets available, i.e.:
195 GEBCO (Monahan, 2008), the Smith and Sandwell bathymetry (Smith and Sandwell 1997) and the ETOPO1 Global Relief Model (Amante and Eakins, 2009) by incorporating new sources of data. We then worked on the optimization of the bottom stress parameterization. Our approach to address the issue of the parametrization and to evaluate the impact of our configuration setup is based on the use of the hydrodynamical model T-UGOm model of
205 Lyard et al. (2006). Thanks to its frequency-domain solver, shortly described in the next sections, T-UGOm can perform tidal simulations at an extremely limited computational cost (compared to time-stepping solver), in our case roughly 80 times faster than usual time-stepping hydrodynamical models (i.e. from few minutes for T-UGOm against hours/days). Furthermore, different formulations for the bottom friction can be prescribed as well as a
210 varying spatial distribution of its related parameters (roughness or friction factor). These particular assets allow to perform a large number of sensitivity tests at a reasonable computational cost on bathymetric and bottom stress parametrization, hence to fasten up the processes of precise tuning and calibration/validation of our configuration.

215 In section 2, we describe the bathymetry, shorelines and waterways construction as well as the numerical model and the modeling strategy in terms of sensitivity experiments. The data used for model evaluation and the metrics used for this evaluation are also presented in this section. In section 3 we present the results regarding the sensitivity of simulations to bottom stress parametrization and to bathymetry. Conclusions and outlook are given in section 4.

2. Methods and tools



2.1 Shorelines and bathymetry construction

The first step of our work is to improve the shoreline and bathymetry precision. Two global digital shorelines are commonly used for representing the general characteristics of the GoT shorelines: the Global Self-consistent, Hierarchical, High-resolution Geography Database (GSHHG, Wessel and Smith, 1996) and the free downloadable maps from OpenStreetMap (OpenStreetMap contributors, 2015; retrieved from <http://www.planet.openstreetmap.org>). The GSHHG and OpenStreetMap shoreline products are both superimposed on satellite and aerial images of the GoT downloaded from Bing (<https://www.bing.com/maps>) and used now as our reference. Fig. 2 shows the shorelines products superimposed on a downloaded image of a small region of the GoT. When closely comparing the shorelines products to the images, it appears that the OpenStreetMap product looks fairly reasonable all along the coastlines of the GoT, except in the Halong Bay area (not shown) where the complex topography and the islets are clearly too numerous. However, the OpenStreetMap shoreline is most of the time shifted by a few meters westwards compared to the land (Fig. 2). The GSHHG dataset suffers from the same problem but shifted by up to 500m eastwards. Our objective in this study is to propose a grid matching the reality as close as possible, therefore, none of these databases looked precise enough to meet our expectations. Consequently, we have built our own shorelines data set, named TONKIN_shorelines, by using the POC Viewer and Processing (POCViP) software (available on the CNRS sharing website, <https://mycore.core-cloud.net/index.php/s/ysqfllcX5njfAYD/download>), developed at LEGOS. The satellite and aerial images of the region, previously downloaded from Bing, are georeferenced with POCViP. The software allows the user to draw nodes and segments with a resolution as fine as needed. The resulting TONKIN_shorelines database has a resolution down to 10m and its accuracy is observable on Fig. 2. We followed the same procedure for building a waterways database of the Red River system. This latter is also included in TONKIN_shorelines. For the Ha Long Bay area, another strategy has been considered since drawing by hand each islet would have been unaffordably time consuming. In this case, images from the Shuttle Radar Topography Mission (SRTM) (<https://earthexplorer.usgs.gov/>) were downloaded and coastlines got extracted and merged to TONKIN_shorelines.

Because of the shallowness of the area, the bathymetry of the GoT is a critical point and



could have a strong impact on tidal simulations as it is often the main constraint in tidal
255 propagation (Fontes et al., 2008). The GEBCO 2014 (30 arc-second interval grid) can be used
to represent the slope and the shape of the basin at a relatively large scale (Fig. 1a,b).
However, its resolution of approximately 1 km is too low to accurately represent detailed
geomorphological features, in particular in coastal regions, near the delta and in the Ha Long
Bay area. In the purpose of providing an improved tidal solution, we have developed a
260 bathymetry with a better precision, named TONKIN_bathymetry (Fig. 1c,d). For that, we
have merged the GEBCO bathymetry with digitalized nautical charts of type CM-93 via
OpenCPM (<https://opencpn.org/>). We also incorporated the tidal flats digital elevation model
from Tong (2016). This author used waterlines from Landsat images of 2014 to construct a
surface model from elevation contours. As tidal flats are suffering tidal regime with
265 submersion during flood tide and exposure during ebb tide, their representation is crucial in
tidal modelling. TONKIN_bathymetry is merged to TONKIN_shorelines dataset.

This scattered bathymetric dataset shows realistic small-scale structures and depths
over the shelf and in the Ha Long Bay area. The details and the islets of the bay are now
represented (Fig. 1c,d), as well as the Red River waterways. In the deeper part of the basin,
270 near the boundary, two deeper branches (in light red) are distinguishable. These latter could
correspond to the location of the ancient river bed of the Red River during the last glacial
time, which split in two around 18°N-108°E (Wetzel et al., 2017). The biggest differences
compared to GEBCO are observed in the central part of the region and in the Hainan Strait
(Fig. 1e,f). In the strait, the GEBCO bathymetry underestimates depths by roughly 20m (~
275 50% in terms of relative difference) compared to TONKIN_bathymetry. In the center,
differences can be up to 30m between the two datasets (not shown on the colorbar),
corresponding to relative differences up to 100%. Such high observed discrepancies are due
to the interpolation of the scattered measuring points from the nautical charts. High relative
differences are also observed all along the coastlines, corresponding for most of them to the
280 integration of the intertidal DEM in the Red River delta area, as well as to a better resolution
in shallow areas obtained from the nautical charts. Discrepancies in most other parts of the
basin remain roughly inferior to 30%. Patches of differences of about 40% between the
datasets are also observed at the open ocean boundary of the domain, with GEBCO also
underestimating depths in the southernmost part.

285 We draw attention to the fact that the TONKIN_bathymetry dataset is not considered here as



the truth, but as an improvement to the available bathymetric dataset; some flaws and uncertainties are remaining and they will be taken into consideration when interpreting the results.

2.2 Model, configuration and forcings

290 2.2.1 T-UGOm hydrodynamic model

The tidal simulations are based on the unstructured grid model T-UGOm (Toulouse Unstructured Grid Ocean Model) developed at LEGOS, and is the follow-up of MOG2D (Carrère and Lyard, 2003). In its standard applications, T-UGOm uses unstructured triangle meshes allowing for an optimal grid resolution flexibility, in particular to discretize complex
295 coastal geometry regions, to follow various local dynamical constraints, such as rapid topography changes or to simply adapt resolution in regions of special interest. The flexibility of unstructured triangle meshes is fully adequate for fine scale modelling, especially in delta or estuarine systems, whereas usual structured meshes may struggle to represent fine geography of certain areas. The T-UGOm model is widely used in global to coastal
300 modelling, mostly for tidal and storm surges simulations: in the representation of semi and quarter-diurnal barotropic tides in the Bay of Biscay (Pairaud et al., 2008), in studying the tidal dynamics of the macro-tidal Amazon estuary (Le Bars et al. 2010) and in assessing the role of the tidal boundary conditions in a 3D model in the Bay of Biscay (Toublanc et al., 2018). Furthermore, T-UGOm has proven its accuracy in global barotropic tidal modelling in
305 the Corsica Channel (Vignudelli et al., 2005) and in a global assessment of different ocean tide models (Stammer et al., 2014).

In addition to its traditional time-stepping solver, it has the remarkable particularity to include a frequency-domain solver kernel, that solves for the 2D/3D quasi-linearized tidal equations. This spectral mode solves the quasi-linearized Navier-Stokes equations in the spectral
310 domain, in a wave by wave, iterative process (to take into account non-linear effects such as bottom friction). It has demonstrated its efficiency (accuracy, computational cost) as well for the astronomical tide simulation as for the non-linear tides. The frequency-domain solver can be used either on triangle or quadrangle unstructured mesh, and therefore can be used on any C-grid configuration. Compared to a traditional time-stepping mode that simulates the
315 temporal evolution of the tidal constituents over a given period, the numerical cost of the



frequency-domain mode (2D) is roughly 1000 times smaller.

For our purpose of assessing the sensitivity to various parameters of the tide representation by the model, T-UGO is set up in a 2D barotropic, quadrangle grid, shallow-water and frequency-domain mode (version of the code: 2616:78a276dd7882 of 2018-07-22
320 13:17 +0200). This configuration is from hereafter named TKN. The main advantage of this fast and reduced-cost-solver is the possibility to perform in an affordable time a wide range of experiments at the regional or global scale, in order to parameterize the model: optimize bottom stress parametrization, test bathymetry improvements and others numerical developments. In our case, the run duration of a spectral simulation with T-UGOm lasts on
325 average 6 mn (CPU time), which is roughly 40 times quicker than a simulation with a regional circulation model such as SYMPHONIE (Marsaleix et al., 2008, CPU time is approximately 4h for a 9-month simulation, corresponding to the required time with SYMPHONIE to separate the tidal waves).

Another useful functionality from T-UGOm for our study is the possibility to locally
330 prescribe the bottom friction, including the roughness length but also the choice of parametrization type. In some shallow coastal regions like the GoT, the presence of fluid mud flow and fine sediments can induce dramatic changes on bottom friction. The quadratic parameterization may be obsolete and a linear parameterization more adequate. This functionality is essential in those particular regions like shallow estuaries, where the
335 influence of bottom friction on the tides propagation is crucial.

2.2.2 Numerical domain over the GoT

The numerical domain over the GoT, built from the TONKIN_bathymetry, is discretized on an unstructured grid made of quadrangle elements (Fig 3). The most commonly used
340 elements in T-UGO are triangles, however here the final goal of our work is to use the resulting grid for coupled hydrodynamical-sediment transport models like SYMPHONIE-MUSTANG (Marsaleix et al., 2008; Le Hir et al., 2011) using quadrangle structured C-grids. We therefore run the T-UGO tidal solver on a quadrangle grid. As in Madec and Imbard (1996), this grid is semi-analytical. A first guess is provided by the analytical reversible
345 coordinate transformation of Bentsen et al (1999) which produces a bipolar grid. The singularities associated with the two poles are located in the continental mask, slightly to the north of the numerical domain, where the horizontal resolution is the strongest (Fig. 3). This



first guess is then slightly modified to control the extension of the grid offshore, in practice to prevent extension beyond the continental shelf. As in Madec and Imbard (1996) this second
350 stage is partly numerical (and preserves the orthogonality of the axes of the grid). The largest edges of the quadrangles are about 5 km at the boundaries of the domain and the smallest of about 150 m long, with a maximum refinement located in the river channels (Fig. 3). This grid allows to represent the complexity of the islets of Ha Long Bay as well as the details of the coastlines of the Red River Delta. A regular C-grid would hardly take into account such
355 complex topography and details.

2.2.3 Tidal open-boundary conditions

For modelling barotropic tidal waves, nine tidal constituents have been imposed as open boundary conditions (OBC) in elevation (amplitude and phase) for our domain: O_1 , K_1 ,
360 M_2 , S_2 , N_2 , K_2 , P_1 , Q_1 and M_4 . These constituents, ordered by their amplitudes (in the GoT), are the main tidal waves in the GoT, and come from the FES2014b global tidal model resolved on unstructured meshes but distributed on a resolution coherent $1/16^\circ \times 1/16^\circ$ grid. FES2014b is the most recent available version of the FES (Finite Element Solution) global tide model that follows the FES2012 version (Carrère et al., 2012). The FES2014b global
365 tidal atlas includes 34 tidal constituents and is based on the resolution of the tidal barotropic equations with T-UGOm (frequency-domain solver for the astronomical tides and time-stepping solver for the non-linear tides, described in the above section). The FES2014b bathymetry has been constructed from the best available (compared to previous FES versions) global and regional DTMs (Dynamical Topography Models), and corrected from
370 available depths soundings (nautical charts, ship soundings, multi-beam data) to get the best possible accuracy, typically 1.3 cm RMS (Root Mean Square error) for the M_2 constituent in the deep ocean before data assimilation. The tidal simulation performed using this configuration and without assimilation is called FES2014b-hydrodynamics. Moreover, in addition to the hydrodynamic solutions, altimetry data-derived and tide gauges harmonic
375 constants have been assimilated, using a hybrid ensemble/representer approach, to improve the atlas accuracy for 15 major constituents and fulfill the accuracy requirements in satellite ocean topography correction. This version of FES will from hereafter be named FES2014b-synthesis in the following, in comparison to FES2014b-hydrodynamics. Thanks to the accuracy of the prior FES2014b-hydrodynamics solutions and the subsequent higher



380 efficiency of data assimilation, this latest FES2014b-synthesis version of the FES2014 atlas
has reached an unprecedented level of precision and has shown a superior accuracy than any
others previous versions (see [http://www.aviso.altimetry.fr/en/data/products/auxiliary-](http://www.aviso.altimetry.fr/en/data/products/auxiliary-products/global-tide-fes.html)
[products/global-tide-fes.html](http://www.aviso.altimetry.fr/en/data/products/auxiliary-products/global-tide-fes.html) and F. Lyard personal comments).

The tidal distribution of the O_1 , K_1 , M_2 and S_2 tidal waves and their first harmonics
385 from FES2014b-synthesis and FES2014b-hydrodynamics is shown in Figs 4ab,5ab,6ab,7ab,
as well as their error along the satellite altimetry track dataset of CTOH-LEGOS (described
below in section 2.3.1). FES2014b-synthesis shows negligible errors compared to FES2014-
hydrodynamics thanks to the assimilation. The main interest of using FES2014-
hydrodynamics in our study is to assess the real capacity of the FES model in reproducing the
390 tidal harmonics without using data assimilation, whereas FES2014b-synthesis can be used
together with satellite altimetry as a reference to evaluate tidal solutions errors.

2.3 Simulations and evaluation

We use the model configuration described above to assess the impact of the improvement of
our bathymetry database and to optimize the representation of bottom friction in the model.
395 For that we perform sensitivity simulations that we compare with available data using
specific metrics. Those tools and methods are presented in this section.

2.3.1 Modelling strategy and sensitivity experiments

The T-UGO 2D model (in its frequency-domain, iterative mode) is run on the high-
400 resolution grid described in section 2.2.2. The following sections describe the tests performed
for the bottom friction parametrization.

2.3.1.1 Bottom stress parametrization

In shallow areas where current intensities are strong due to a macro-tidal environment
405 combined to strong rivers flows and winds forcing, the sensitivity of the model to the bottom
stress is significant. The bottom stress is thus a crucial component for modelling nearshore
circulation and sediment transport dynamics (Gabioux et al. 2005; Fontes et al., 2008). The
bottom stress formulation depends upon a non-dimensional bottom drag coefficient (or
friction coefficient) C_D and can be obtained as follows, in barotropic mode:



410

$$\tau_b = \rho C_D |\bar{u}| \bar{u} \quad (1a)$$

with \bar{u} the depth averaged velocity and ρ the fluid density.

415 In the case of the presence of fluid mud, the bottom friction is purely viscous and the velocity profiles are linear, Gabioux et al. (2005) described the τ_b as follows:

$$\tau_b = \rho r \bar{u} \quad (1b)$$

420 with r corresponding here to the friction coefficient.

In this study, we test three commonly used parameterizations: a constant drag coefficient C_D assuming a constant speed profile or a linear speed profile, and a drag coefficient C_D depending upon the roughness height z_0 .

425 In the first parameterization, a constant profile of the speed is assumed over the whole water height, leading to quadratic bottom stress and a constant C_D that depends on the Chézy coefficient C and on the acceleration due to gravity g (Dronkers 1964):

$$C_D = \frac{g}{C^2} \quad (2)$$

430

In the second parameterization, a linear profile of the speed is assumed over the whole water column which characterizes viscous conditions. In this case, a linear bottom stress is assumed and r depends on the frequency of the forcing wave ω (here Ω_i) and the fluid kinematic viscosity ν :

435

$$r = \sqrt{\omega} \nu \quad (3)$$

In the third parameterization, a logarithmic profile of the speed is assumed over the whole water column (Soulsby et al. 1993), leading to a C_D depending upon the roughness length z_0 ,
440 the total water height H and the von Karman's constant $\kappa=0.4$:



$$C_D = \left(\frac{\kappa (H - z_0)}{H \ln \frac{H}{z_0} + z_0 - H} \right)^2 \quad (4)$$

445 The roughness length z_0 (also called roughness height) depends not only on the morphology
of the bed (i.e. the presence of wavelets or not) but also on the nature of the bottom sediment.
In presence of fluid mud, the friction is considered as purely viscous (Gabioux, 2005).
However, the repartition of sediments and the structure of the sea bed are not uniform over
the GoT shelf as the Red River discharge causes patches of sediments of different natures
450 (Natural Conditions and Environment of Vietnam Sea and Adjacent Area Atlas, 2007).
Consequently, we can expect z_0 to vary spatially. This issue can be addressed with T-UGOm
since it contains a domain partition algorithm allowing to take into account the spatial
variability of the sea bed roughness. Furthermore, this C_D parameterization which includes a
logarithmic profile of the speed, allows to adapt the C_D to the model vertical resolution by
455 considering the water column depths, as a way to correspond to the friction coefficient
resolution in 3D models.

In this study, these three C_D formulations of the coefficient of friction (Eqs. 2, 3 and 4) are
tested for model parameterization, varying respectively the value of C_D , the value of r and the
value of z_0 .

460 2.3.1.2 Sensitivity to uniform friction parameters

Sensitivity numerical experiments were first conducted in order to assess the sensitivity of the
model to uniform parameters of friction for two of the parameterizations described above: a
quadratic bottom stress with a uniform drag coefficient C_D (Eqs. 1a and 2) and a logarithmic
465 variation of C_D depending on a uniform bottom roughness height z_0 (Eq. 4). For that, we
performed a first set (SET1) of 45 tests running the model with a constant C_D with C_D values
spanning from 0.5×10^{-3} to 5.0×10^{-3} m (see Fig. 8 where we plotted C_D values spanning from
 0.5 to 2.5×10^{-3} m). We then performed a second set (SET2) of 6 tests running the model with
a logarithmic C_D by testing values from 1.0×10^{-1} to 1.0×10^{-6} m for z_0 (see Fig. 9).



470 2.3.1.3 Sensitivity to the regionalization of the roughness coefficient

As mentioned in the previous section, a uniform roughness coefficient does not usually allow for reaching a satisfying level of accuracy over the whole domain, since the variability of the seafloor morphology is not fully taken into consideration. To take this
475 variability into account, the spatial variability of the seabed roughness must be prescribed to the model. For that, our study area is divided into several zones based on seabed sediment types repartition obtained from the Natural Conditions and Environment of Vietnam Sea and Adjacent Area Atlas (2007).

The third set of sensitivity experiments (SET3, tests A to E in Table 1) consisted in
480 prescribing a linear velocity profile only in the area of fine mud, following Eqs. 1b and 3, with a fixed $r = 1.18 \times 10^{-4}$ m (see Fig 10a), and to test different values of uniform z_0 (from 1.0×10^{-2} to 1.0×10^{-6} m) over the rest of the region, prescribing a logarithmic velocity profile. This value of r is taken from the value empirically tuned on the region of the Amazon estuary and shelf with the configuration described in Le Bars et al. (2010)

485 The fourth set of sensitivity experiments (SET4, tests 1 to 7 in Table 1) consisted in dividing the region into three zones, according to a supposed spatial distribution of the seabed sediments, inspired from the above-mentioned Vietnamese atlas (Fig. 10b): zone 1 is mostly composed of muddy sand, zone 2 of mud and zone 3 of sand and coarser aggregates. In each zone, a value of z_0 (from 1.0×10^{-2} to 1.0×10^{-5} m) is prescribed following a logarithmic speed
490 flow (Eq. 4). Note that for this set of experiments every combinations of z_0 were tested, yet for the sake of clarity we show and describe in the section 4 only the ones with errors (see section 2.3.3) for S_2 solutions below 2.5 cm.

The fifth and last set of experiments (SET5) consisted in dividing the domain into twelve zones, in order to refine the representation of the spatial distribution of the seafloor's
495 sediments following the Vietnamese atlas (Fig. 10c). Zones 1 and 11 correspond to muddy sand; zones 2, 6, 10 and 12 to sand slightly gravel; zones 3 and 5 to sandy mud; zone 4 to fine mud; zone 7 to sandy gravel; zone 8 to mud slightly gravel; and zone 9 to sand. Different z_0 values (varying from 1.0×10^{-2} to 1.0×10^{-5} m), using a logarithmic velocity profile, were prescribed to each of the 12 zones and corresponding run were performed, each time
500 imposing a random and different value to each zone.



2.3.2 Satellite data for model assessment

The evaluation of the performance of the simulations is made with along-track tidal harmonics obtained from a 19-year (1993 - 2011) long time series of satellite altimetry data available every ten days from TOPEX/Poseidon (T/P), Jason-1, and Jason-2 missions (doi: 10.6096/CTOH_X-TRACK_Tidal_2018_01). These data are provided by the CTOH-LEGOS (Birol et al., 2016). The tracks of the altimeters passing over the GoT are shown in Fig. 4 to 7, and are spaced by approximately 280 km. To complement those data in the intertrack domain, we also compare our simulations with the FES2014b-synthesis tidal atlas, as explained in section 2.2.3.

2.3.3 Metrics

For comparison of the simulations with the tidal harmonics from satellite altimetry, two statistical parameters (metrics) are used. These are the root mean square error (RMS*) and the mean absolute error (MAE). The RMS* computation is based on a vectorial difference which combines both amplitude error and phase error into a single error measure. The errors computations are detailed in Appendix.

3. Results

In this section we present the results concerning the sensitivity of the modeled tidal solutions to the choice of bathymetry dataset and to the choice of bottom friction parameterization. Spatially varying uniform friction parameters induce the best results on the tidal solutions rather than uniform parameters. However, prescribing a linear parameterization in supposed fluid mud areas does not allow to significantly improve the solutions, unlike in Le Bars (2010). Lastly, the reconstructed bathymetry dataset allows to strongly improve the semi-diurnal tidal solutions. The improvements consist mainly in a correction near the coasts and in reducing the errors in phase (as it can be expected from a bathymetry upgrade). We present the results of the conducted sensitivity experiments in details in the following sub-sections.



3.1 Bottom stress and roughness length model sensitivity

530 3.1.1 Sensitivity to the value of spatially uniform parameters (SET1 and SET2)

We first analyse in this section and in the next one the sensitivity to the parameterization of bottom friction. Firstly, to show the sensitivity to the choice of uniform friction parameters, the model errors (Appendix; Eq. 6) compared to satellite altimetry are shown in Fig. 8 (SET1) and 9 (SET2), for the main tidal constituents (O_1 , K_1 , M_2 , S_2) for each values of uniform C_D and z_0 tested in SET1 and SET2 described in section 2. On both Figs. 8 and 9, the space in between two solid lines corresponds to the errors for the considered wave (see legend) and the yellow line represents the cumulative errors for the four waves. The dashed red line represents the smallest cumulative error (i.e. the minimum value reached for the yellow line).
540 yellow line).

First of all, the diurnal waves O_1 and K_1 are more affected by the changes in the values of C_D and z_0 than the semi-diurnal waves M_2 and S_2 (Figs. 8 and 9). This can be explained by the fact that diurnal tides are of greater amplitude than semi-diurnal in the Gulf of Tonkin, thus the tidal friction is truly non-linear for O_1 and K_1 and marginally only for M_2 and S_2 . For C_D values below 0.6 and above 1.0×10^{-3} m, O_1 and K_1 errors are larger than errors for M_2 and S_2 . For example, for $C_D = 2.5 \times 10^{-3}$ m the errors for O_1 are roughly 4 to 11 times larger than errors for M_2 and S_2 and errors for K_1 are roughly 3 to 10 times larger than errors for M_2 and S_2 , respectively).
545 values below 0.6 and above 1.0×10^{-3} m, O_1 and K_1 errors are larger than errors for M_2 and S_2 . For example, for $C_D = 2.5 \times 10^{-3}$ m the errors for O_1 are roughly 4 to 11 times larger than errors for M_2 and S_2 and errors for K_1 are roughly 3 to 10 times larger than errors for M_2 and S_2 , respectively).

Small values of C_D also induce large errors of O_1 and K_1 (for $C_D = 0.5 \times 10^{-3}$ m, errors for O_1 are roughly 1.5 to 3.8 times larger than errors for M_2 and S_2 , and errors for K_1 are roughly 2.8 to 6.9 times larger than errors for M_2 and S_2 , respectively). High and small values of z_0 also trigger larger errors on the diurnal waves (Fig. 9).
550 roughly 1.5 to 3.8 times larger than errors for M_2 and S_2 , and errors for K_1 are roughly 2.8 to 6.9 times larger than errors for M_2 and S_2 , respectively). High and small values of z_0 also trigger larger errors on the diurnal waves (Fig. 9).

Secondly, the tests of sensitivity to a spatially constant friction coefficient C_D show that the lowest error is reached for $C_D = 0.9 \times 10^{-3}$ m (the cumulative error is equal to 11.50 cm) (Fig. 8). This value of C_D is roughly half lower than those used for the whole South China Sea (2.0×10^{-3} m: Fang et al. 1999; Cai et al., 2005) and similar to the one used in the GoT by Nguyen et al. (2014) of 1.0×10^{-3} m. The tests of sensitivity to the roughness length z_0 show that the value $z_0 = 1.5 \times 10^{-5}$ m yields the least errors (the cumulative error is equal to 10.96 cm) (Fig. 9). This is a relatively small roughness length value, indicating a sea bed composed of very fine particles. Note that, the use of a constant C_D parametrization with a C_D of 0.9×10^{-3} m
560 very fine particles. Note that, the use of a constant C_D parametrization with a C_D of 0.9×10^{-3} m



or a constant roughness length with a z_0 of 1.5×10^{-5} m leads to almost identical errors (0.54 cm of differences). These rather low values of friction and roughness coefficients suggest the presence of a majority of fine sediments in the GoT. This is consistent with the results from Ma et al. (2010), who found the western and central parts of the GoT to be mainly composed
565 of fine to coarse silts, with a few patches of sand next to Hainan island.

Thirdly, the lowest error for each wave is reached for different values of C_D and z_0 . In SET1, the lowest error value for O_1 is reached when $C_D = 0.9 \times 10^{-3}$ m, while the lowest error value for K_1 is reached for $C_D = 1.0 \times 10^{-3}$ m. The lowest errors values of the semi-diurnal waves are reached for $C_D = 1.4 \times 10^{-3}$ m (Fig. 8). In SET2, the lowest errors values of the diurnal waves
570 are reached for $z_0 = 1.5 \times 10^{-5}$ m and are reached for $z_0 = 1 \times 10^{-3}$ m for the semi diurnal waves (Fig. 9). This finding is of course unphysical, and the reader must keep in mind that optimal parameter setting also often deals with model errors numerical compensation. In our study, it is quite obvious that the model bathymetry is far from perfect despite the large efforts carried out to improve the topographic dataset, and remaining errors due to bathymetry imperfections
575 can be partly canceled by the use of an adequate (i.e. numerical, not physical) friction parameter. As bathymetry-induced errors will strongly be affected by the tidal frequency group (species), and since bathymetry directly and distinctly impacts the waves' phase propagation, we can expect that optimal friction parameterization alteration (and corresponding alterations of the bottom shear stress) will slightly vary in a given frequency
580 group but strongly from one to another. The examination of sensitivity studies tends to promote the idea that these differences are mostly due to remaining errors in the bathymetric dataset and the final decision for an optimal friction parameterization will be based on the best compromise for the overall solution errors. As the K_1 and O_1 sensitivity to friction alteration is prevailing, the compromise is of course mostly driven by these two tidal waves.

585 3.1.2 Sensitivity to the value of spatially varying roughness length (SET3, SET4, SET5)

The results of the tests performed to assess the model sensitivity to a regionalized roughness coefficient (see Table 1) are shown in Fig. 11.

No significant improvement of the tidal solutions is obtained from SET3, i.e. by imposing a
590 linear flow in the mud region (where the resolution is the highest), compared to the tests performed with spatially uniform parameters (drag coefficient, SET1 and bottom roughness length, SET2, Figs. 8 and 9). The cumulative error of all four waves (yellow line) is always



above the 10.96 cm value of the smallest error found for SET2 (the smallest cumulative error of 11.33 cm is obtained for test C). Results from SET3 (Tests A to F) show that the solutions
595 still greatly depends upon the roughness length values imposed to the rest of the region, with errors increasing with low and high values of z_0 : from tests D to G, cumulative errors increase by a factor 3.5 with z_0 values increase from 1×10^{-4} to 1×10^{-1} m; from test A to B, errors decrease by a factor 2 with values decreasing from 1×10^{-6} to 1×10^{-5} m. As previously observed, the diurnal waves O_1 and K_1 (in tests A to F) are more sensitive to changes in z_0
600 than the semi-diurnal M_2 and S_2 waves: for $z_0=1 \times 10^{-2}$ m, errors of O_1 are 3 and 7 times larger than errors of M_2 and S_2 respectively, and errors of K_1 are 4.5 to 11 times larger than errors of M_2 and S_2 , respectively.

Significant improvement of the tidal solutions is obtained from SET4, i.e. by varying
605 spatially the values of the bottom roughness length (imposing a logarithmic speed profile). The cumulative error of all four waves (yellow line) reach a minimum value of 10.43 cm for Test 6 (red dashed line), which reduced the error found in SET2 by 0.53 cm. This value is reached by imposing values of $z_0=1.5 \times 10^{-5}$ m in regions 1 and 2 (Fig. 10) and $z_0=1 \times 10^{-4}$ m in region 3. Moreover, results from Test 1 and Test 2 show that the solutions largely depend
610 upon the roughness length imposed in region 1 (z_0 values of 1×10^{-2} to 1×10^{-3} m). Again, as already mentioned in the previous section, the remaining bathymetry-induced errors in our solutions have probably damaged the precise identification of truly physical friction parameterization in this spatially varying roughness length experiment.

615 Lastly, the results of the tests from SET5 did not show any improvement on the tidal solutions, compared to SET3 and SET4. The minimum cumulative error found in SET5 is equal to 12.29 cm and is 15% times larger than the minimum cumulative error found for test 6 in SET4 (Fig. 11) (Figures not shown for the sake of conciseness and clarity). These results suggest that the model seems to be insensitive to high spatial refinement of the bottom
620 sediment composition and associated roughness for the representation of tidal solutions.

3.2 Sensitivity to the bathymetry and assessment of tidal solution

Model bathymetry is a key parameter for tidal simulations. In order to evaluate the sensitivity of the model to the bathymetry, an additional sensitivity simulation is performed.



625 First, the solutions obtained with the grid configuration with improved bathymetry and
shoreline datasets described in section 2.1 (Fig. 3) and a spatially varying roughness length
(described in Test 6, Table 1) with a logarithmic velocity profile are chosen as this choice of
bottom roughness parameterization has shown the best tidal solutions (the least errors to
satellite altimetry) in section 3.1.2. This simulation is named TKN hereafter. Second, we run
630 a twin simulation with exactly the same configuration, parameterizations and choice of
parameters, except that the bathymetry and shoreline are not built from our improved dataset
but from the default GEBCO bathymetry dataset and default-shoreline dataset. This
simulation is hereafter named TKN-gebco. The results from these tests are presented in this
section, where we evaluate the quality of the tidal solution obtained in our different
simulations.

635 3.2.1 Average assessment over the domain

We first evaluate the tidal solution in average over the domain. Integrated alongtrack RMS*
errors (Appendix; Eq. 6) between modelled and observed tidal harmonics are shown in Fig.
12. FES2014b-synthesis errors are globally always lower than errors given by the three other
640 simulations, thanks to the assimilation of the satellite altimetry: 3 to 4.7 times lower for O_1 ,
2.6 to 3.2 times for K_1 , 2.3 to 3.7 times smaller M_2 and 1.3 to 2.7 times for S_2 . As explained
in section 2.2.3, FES2014b-synthesis, which minimizes the error, is used in the following as a
reference for the evaluation of our simulations to spatially complement altimetry data which
are only available along the altimetry tracks.

645 Alongtrack RMS* errors for M_2 are reduced by 12% in TKN-gebco relative to FES2014b-
hydrodynamics and by 47% in TKN. The errors are also lower for S_2 , with a reduction of the
errors by 41% between FES2014b-hydrodynamics and TKN-gebco, and by 56% between
FES2014b-hydrodynamics and TKN. On the other hand, both TKN and TKN-gebco
simulations show bigger errors than FES2014b-hydrodynamics for O_1 and K_1 . However,
650 TKN simulation increases the errors for O_1 by 7% relative to FES2014b-hydrodynamics
whereas TKN-gebco increases the errors by 58%. The complex errors for K_1 obtained from
both TKN and TKN-gebco simulations increase by roughly 12 and 20% compared to
FES2014b-hydrodynamics, respectively. Such results illustrate the fact that K_1 wavelengths
are longer than the other waves' wavelengths considered here, e.g.: at 60 m depth, K_1
655 wavelength is 2000 km and M_2 wavelength is 1000 km (Kowalik and Luick, 2013), therefore



K_1 is less sensitive to bathymetric variations.

Furthermore, the mean absolute differences MAE (Appendix; Eq. 7) of amplitude and phase of the four tidal constituents between our simulation TKN and the satellite altimetry are given in Table 2. Our results are compared with the errors given in Minh et al. (2014) and in Chen et al. (2009). Minh et al. (2014) authors used a ROMS_AGRIF simulation at a resolution of $1/25^\circ \times 1/25^\circ$ over the GoT, and compared their solutions to the same altimetric dataset as the one used in our study. Chen et al. (2009) compared their simulations, performed with ECOM (Extended Control Model) at a 1.8×1.8 km resolution (covering the area 16°N - 23°N , 105.7°E - 114°E), to gauge stations located along the GoT coast. Our simulation TKN shows large improvements in both amplitude and phase for the four constituents (except for the phase of M_2) compared to the results of Minh et al. (2014). The errors are reduced by approximately 60% for the amplitudes of M_2 and S_2 approximately, and by roughly 40% for the amplitudes of K_1 and O_1 , respectively. The errors in phase for O_1 and K_1 are also reduced by approximately 50% in our simulation. Our results show also improvements compared with the errors proposed by Chen et al. (2009), for both amplitude and phase of S_2 (by 65% in amplitude and by 35% in phase), O_1 (by 50% in amplitude and almost 60% in phase) and K_1 (by 68% in amplitude and by 41% in phase). Only the solutions of M_2 are not improved by our simulation compared to Chen et al. (2009): they remain the same in amplitude and increase by 14% in phase.

3.2.2 Spatial assessment of tidal solutions

The modelled O_1 , K_1 , M_2 and S_2 fields for TKN, TKN-gebco, FES2014b-hydrodynamics and FES2014b-synthesis are shown in Figs. 4 to 7. For each tidal component and simulation, the complex errors RMS* between these simulations results and the tidal harmonics extracted from satellite altimetry data are represented for each point of the altimetry track by the circles superimposed on the maps.

Both model simulations (TKN-gebco and TKN) reproduce well the distribution patterns of O_1 harmonics compared to FES2014b-synthesis, improving the results compared to FES2014b-hydrodynamics. Moreover, TKN solutions look more accurate than TKN_gebco. Errors to SLA for O_1 (circles on the maps) are smaller than 10 cm in TKN_gebco and are reduced by 35% compared to FES2014b-hydrodynamics. They are further reduced in TKN: most of the



errors are smaller than 5 cm and are reduced by 50% compared to FES2014b-hydrodynamics (Fig. 4). Note that higher errors of SLA (of about 20cm) are observed in TKN and TKN-gebco in the Hainan Strait and also near the coasts. These errors also appear in FES2014b-hydrodynamics and, to a lesser extent (with values of about 15 cm in the Hainan Strait) in FES2014b-synthesis. The increase of complex errors in these particular areas could be explained by either model errors associated with errors in coastal bathymetry and shorelines, whose accuracy is decisive to shallow water tidal wave and/or to erroneous altimetric data (land contamination in the altimeter footprint). For K_1 , even though both model simulations reproduce well the distribution pattern of the harmonics compared to FES2014b-synthesis, the errors to SLA compared to FES2014b-hydrodynamics are not reduced in TKN-gebco nor in TKN (Fig. 5). Errors to SLA for K_1 are equals or smaller than 10 cm in FES2014b-hydrodynamics, TKN-gebco and TKN along the altimetry tracks, and are extremely similar between those simulations. As observed for O_1 , larger and similar errors of about 20 cm are also observed in the Hainan Strait in TKN-gebco and TKN and in the two FES2014b products (though with smaller values of about 15 cm in FES2014b-synthesis that includes assimilations). Furthermore, the angle of the circles' radius indicates which of the error in amplitude or the error in phase dominates the complex error. The smaller the angle is to the ordinate axis, the more the error in phase dominates the complex error. On the contrary, the bigger the angle is to the ordinate axis, the more the error in amplitude dominates the complex error. When the angle to the ordinate axis approaches 45° , the error in phase and the error in amplitude account equally for the complex error. For both O_1 and K_1 , errors in phase are dominating the northern and central parts of the region, while the phase and amplitude account equally for the complex errors in the southernmost part of the region and in the Hainan Strait (Fig 4cd;5cd).

Fig. 6 shows that M_2 amplitude is globally overestimated by TKN and TKN-gebco compared to FES2014b-synthesis and FES2014b-hydrodynamics, especially in the areas where the wave resonates (i.e. in the north eastern bay and in the south-western part). Differences to FES2014b-hydrodynamics are up to 30 to 35 cm in TKN and in TKN-gebco (in the north-eastern bay), with amplitudes increasing by almost 45% in model simulations. Both model simulations increase the resonance of M_2 in the bays. However, the amplitudes are underestimated near the amphidromic point (20.7°N , 107.3°E) by both simulations compared



720 to FES2014b-hydrodynamics (by up to 10 cm, roughly 80%). Globally, errors to SLA are
reduced in TKN by 30% compared to TKN-gebco: most of the errors in TKN are smaller
than 10 cm while most of the errors in TKN-gebco are equals or larger than 10 cm. Both
simulations show also smaller errors to SLA south of Hainan Island compared to FES2014b-
hydrodynamics by up to 50%, with errors of about 1 cm in FES2014b-hydrodynamics and of
725 about 0.5 cm in model simulations). Again, large errors are observed in the Hainan Strait in
simulations and both FES2014b products, however the errors are reduced by 25% in TKN
and TKN-gebco compared to FES2014b-hydrodynamics. Furthermore, these errors are
dominated by errors in phase rather than in amplitude.

730 Lastly, both TKN and TKN-gebco model simulations overestimate the amplitude of S_2
compared to FES2014b-synthesis and FE2014b-hydrodynamics by up to 10 cm
(approximately 50%) in the south-western and north-eastern bays, where S_2 resonates (Fig.
7). The resonance of S_2 in the bays is therefore amplified in both model simulations.
Similar to M_2 case, both simulations also underestimate by roughly 5 cm the amplitude of S_2
735 near the amphidromic point (20.7°N, 107.3°E) compared to the two FES2014b products.
However, the complex errors to SLA are globally 50% smaller in TKN (between 2 to 3 cm)
than in TKN-gebco (between 4 to 5 cm). Furthermore, errors to SLA remain large in the
Hainan Strait (up to 6 cm) in both FES products and both model simulations. In the very near
coastal areas, errors to SLA in TKN and TKN-gebco are larger than in the rest of the basin
740 (up to 6 cm). However, the errors to SLA in TKN are reduced by 30% in the south-western
most part of the region. Like M_2 case, the complex errors of S_2 are dominated all over the
basin the by errors in phase rather than errors in amplitudes.

4. Conclusions

745

This study takes place in the framework of a more comprehensive modeling project which
aims at representing the transport and fate of the sediments from the Red River to the GoT. In
this future study, the ocean dynamics and the sediments transport will be represented using
the regional circulation model SYMPHONIE coupled with the sediment model MUSTANG.
750 As tides have a major effect on the sediment dynamics within the estuaries and in the plume
area (Pritchard 1954, 1956; Allen et al., 1980; Fontes et al., 2008; Vinh et al., 2018), it is



necessary to accurately represent the tidal processes before investigating the fine scale sediment physics. Optimizing the bathymetry and the parameterization of the bottom shear stress is crucial in shallow-water regional and coastal modeling since they both are critical parameters influencing the propagation and distortion of the tides (Fontes et al., 2008; Le Bars et al., 2010). The T-UGO hydrodynamical model is used in this study in its spectral mode, which allows the user to perform fast and low-cost tests (compared to simulations with SYMPHONIE) on various parameterizations and bathymetry configurations. This strategy allows to assess and quantify the importance of each element considered and to determine the best configuration and parameterization that will be applied in the above-mentioned forthcoming modeling study with SYMPHONIE-MUSTANG model.

In this study, we have first constructed an improved bathymetric dataset for the region of the GoT from digitalized nautical charts, soundings, intertidal DEM and GEBCO bathymetry dataset. We also integrated to this bathymetry a new coastline dataset created with POCViP and satellite images, since the existing descriptions of the GoT coastlines, the Ha Long Bay islets and the Red River delta were very poor. We then performed tests with the fast-solver 2D T-UGOm model on an unstructured grid refined in the Red River delta and Ha Long Bay area to test the added value of this improved bathymetric dataset. With this new bathymetry, we have been able to reduce the errors (taking alongtrack altimetry data as a reference) of the representation of M_2 and S_2 in T-UGOm simulations by 40% and 25% respectively and O_1 and K_1 by 32% and 6% respectively, compared to simulations that use the regular GEBCO dataset. Our improved bathymetry showed also better solutions for the semi-diurnal waves than the tidal atlas FES2014b_hydrodynamics (errors reduced by 47% for M_2 and by 25% for S_2), even though our model seems to amplify their resonance. Moreover, our simulations also improved accuracy over the existing state of the art, by reducing the errors in amplitude of the semi-diurnal waves by 60%, the errors in amplitude of the diurnal waves by 40%, and the errors in phase of the diurnal waves by 50% compared to the results found by Minh et al. (2014). We believe the remaining errors in our best tidal solutions are due to potential lacks of details and resolution in the bathymetric dataset. Since bathymetry directly impacts the waves' speeds, bathymetric uncertainties may lead to alterations of the bottom shear stress.

The other key parameter influencing shallow-water tidal modelling is the bottom friction. In



785 this study, the use of a constant C_D parametrization or the use of a C_D depending on the
roughness length led to fairly similar results, in line with the results found by Le Bars et al.
(2010) in the Amazon estuary. Furthermore, our study shows that the model is very sensitive
to the values imposed to C_D and z_0 , especially for the diurnal waves with errors increasing for
extreme C_D and z_0 values. The lowest cumulative errors of all four waves (of 11.50 and
10.96cm) were found for a uniform C_D of 0.9×10^{-3} m (prescribing a constant velocity profile)
790 and for a uniform z_0 of 1.5×10^{-5} m (prescribing a logarithmic velocity profile), respectively.
More importantly, the regionalisation of the roughness length into three regions, for
addressing the issue of representing the complexity of seabed composition and morphology,
moderately improved the accuracy of our simulation, with a lowest cumulative error for all
four waves of 10.43 cm. Finer local adjustments of the roughness length or the choice of a
795 linear velocity profile in the area of fine mud, did not improve the accuracy of our
simulations. In particular, the model in this configuration showed a very limited sensitivity to
the presence of fine mud and a greater sensitivity to the roughness length values prescribed in
the rest of the region.

800 Our results therefore quantitatively showed the importance of the bathymetry and shoreline
dataset and of the choice of bottom friction parameters for the representation of tidal
simulations over a shallow area like the GoT. Furthermore, the use of T-UGOm in a 2D
barotropic mode showed its efficiency in tidal spectral modelling with reduced simulation
durations in both CPU and running times compared to structured grid numerical models. This
805 allowed us to optimize our configuration in terms of grid, bathymetry and bottom friction
parameterization regarding the representation of the tidal solutions. Our resulting
configuration brought a clear improvement in the tidal solutions compared to previous 3D
simulations from the literature and to the tidal atlas FES2014b (without data assimilation) for
the semi-diurnal waves. The modeling strategy proposed here showed its efficiency in
810 quickly optimizing the configuration that will be used in future works to address the issue of
sediment transport and fate in the GoT.

Using bathymetry data available from digitalized navigation charts was a relatively simple
way (compared to performing additional in-situ measurements) to significantly improve the
815 representation of topography in the coastal and estuarine areas of the GoT, and could be



applied successfully in other regions. However, updates and improvements in shorelines and bathymetry databases, particularly in the river channels, coastal areas and in the Hainan strait would still improve the present results and especially reduce the tendency to increasing errors at the coasts. Continuous efforts should be made in bathymetric data acquisition and sharing
820 them with the community should be a crucial concern.

Code and/or data availability:

The model grid, which integrates the bathymetry and the coastline datasets developed in this study, is available for download via <https://zenodo.org/record/2640763#.XLSBcJzgreM>. The T-UGO model code installation instructions are updated at <ftp://ftp.legos.obs-mip.fr/pub/ecola/README.html>, and
825 the code, as well as the updated tools and the poc-solvers are available on <https://hg.legos.obs-mip.fr/tools/>. An archive of the exact version of T-UGOm used in this study (version 2616:78a276dd7882) is also available on <https://zenodo.org/record/2669397#.XNBDLJzgreM>. The configuration files (initial conditions and modified drag coefficients) are available on <https://zenodo.org/record/2640793#.XLSGYZzgreM>. Model boundary conditions (i.e. FES2014
830 products) are available through: <https://www.aviso.altimetry.fr/en/data/products/auxiliary-products/global-tide-fes.html>. The satellite altimetry track dataset of CTOH-LEGOS for model outputs comparison are available through: <http://ctoh.legos.obs-mip.fr/products/coastal-products/coastal-products-1/sla-1hz> (doi: 10.6096/CTOH_X-TRACK_Tidal_2018_01).

Authors contribution:

835 VP, MH, SO and FL designed the experiments and VP carried them out. FL developed the model code and VP performed the simulations. VP, TH and DA constructed the bathymetry dataset. VP prepared the manuscript with contributions of MH, FL, SO and PM.

Acknowledgments:

Map data copyrighted OpenStreetMap contributors and available from
840 <https://www.openstreetmap.org>. We thank the CTOH team of LEGOS (Toulouse) for providing coastal altimetry data. This paper is a contribution to the LOTUS International Joint Laboratory (lotus.usth.edu.vn).



Appendix:

For comparison of the simulations with the tidal harmonics from satellite altimetry, we first
 845 introduce the vectorial difference z , or complex difference, as:

$$z = z_m - z_o \quad (5)$$

with $z_m = A_m e^{iG_m}$ the vector representing a given modelled tidal constituents (of amplitude A_m
 850 and phase G_m) and z_o the vector representing the observed tidal constituent.

For assessing the errors between the simulations (modelled constituents) and the altimetry
 (observed constituents), we compute the root mean square error (RMS*), like in Stammer et
 al. (2014) and in Minh et al. (2014). RMS* depends upon the vectorial difference z and is
 855 computed for each given constituent of each simulation, as follows:

$$RMS = \sqrt{\left(\frac{1}{N} \sum_{i=1}^N 0.5 |z|^2 \right)}$$

$$RMS = \sqrt{\left(\frac{1}{N} \sum_{i=1}^N 0.5 \left[(A_m \cos(G_m) - A_o \cos(G_o))^2 + (A_m \sin(G_m) - A_o \sin(G_o))^2 \right] \right)} \quad (6)$$

with A_m and G_m being respectively the amplitude and phase of the modelled constituent, A_o
 860 and G_o , the amplitude and phase of the constituent from satellite altimetry and N the number
 of points of comparison (i.e. the number of equivalent gauge stations along the altimetry
 tracks).

The model performance is also estimated using the mean absolute error (MAE). MAE
 865 measures the mean of the difference between the simulated and the observed values and is
 computed for each constituent according to:

$$MAE = \frac{\sum_{i=1}^N |E_i|}{N} \quad (7)$$

with E_i representing for each point i of the track the difference between the modeled
 870 constituent and the observed constituent. The MAE is separately calculated for amplitudes
 and for phases.



References

Allen G. P., Salomon J. C., Bassoullet P., Penhoat Y. D., Grandpré C.: Effects of tides on mixing and suspended sediment transport in macrotidal estuaries *Sediment. Geol.*, 26(1-3), 875 69-90, 1980.

Amante C., Eakins B. W.: ETOPO1 1 Arc-Minute Global Relief Model: Procedures, Data Sources and Analysis. NOAA Technical Memorandum NESDIS NGDC-24, National Geophysical Data Center, NOAA, doi: 10.7289/V5C8276M, 2009.
880

Bentsen M., Evensen G., Drange H., Jenkins A. D.: Coordinate Transformation on a Sphere Using Conformal Mapping, *Month. Weath. Rev.*, 2733-2740, 1999

Birol F., Fuller N., Cancet M., Nino F., Delebecque C., Fleury S., Toublanc F., Melet A., 885 Saraceno M., Léger F.: Coastal applications from nadir altimetry: example of the X-TRACK regional products, *Adv. Space Res.*, 59, 936-953, doi: <http://dx.doi.org/10.1016/j.asr.2016.11.005>, 2016.

Cai S., Long X., Liu H., Wang S.: Tide model evaluation under different conditions. *Cont. Shelf. Res.*, 26, 104-112, 2005.
890

Carrère L., Lyard F.: Modeling the barotropic response of the global ocean to atmospheric wind and pressure forcing - comparison with observations, *Geophys. Res. Lett.*, 30(6), 1- 4, doi:10.1029/2002GL016473, 2003.
895

Carrère L., Lyard F., Cancet M., Guillot A., Roblou L.: FES2012: a new global tidal model taking advantage of nearly 20 years of altimetry, *Proceedings of 20 years of Altimetry*, Venice, 2012.

900 Chen C., Li P., Shi M., Xuo J., Chen M., Sun H.: Numerical study of the tides and residual currents in the Leizhou Strait, *Chin. J. Oceanol. Limnol.*, 27(4), 931-942, 2009.

Dang T. H., Coynel A., Orange D., Blanc G., Etcheber H., Le L. A.: Long-term monitoring



- (1960-2008) of the river-sediment transport in the Red River Watershed (Vietnam): Temporal
905 variability and dam-reservoir impact, *Sci. Total Environ.*, 408, 4654-4664, doi:
10.1016/j.scitotenv.2010.07.007, 2010.
- Debreu L., Marchesiello P., Penven P., Cambon G.: Two-way nesting in split-explicit ocean
models: algorithms, implementation and validation, *Ocean Model.* 49-51, 1-21, doi:
910 <http://dx.doi.org/10.1016/j.ocemod.2012.03.003> , 2012.
- Ding Y., Chen C., Beardsley R. C., Bao X., Shi M., Zhang Y., Lai Z., Li R., Lin H., Viet N.
T.: Observational and model studies of the circulation in the Gulf of Tonkin, South China
Sea, *J. Geophys. Res.*, 118, 6495-6510, doi:10.1002/2013JC009455, 2013.
915
- Dronkers J.J.: *Tidal Computations in Rivers and Coastal Waters*, North-Holland,
Amsterdam. 1964.
- Eyre B., McConchie D.: Implications of sedimentological studies for environmental pollution
920 assessment and management: examples from fluvial systems in North Queensland and
Western Australia, *Sediment Geol.*, 85, 235-252, 1993.
- Fang G.: Tide and tidal current charts for the marginal seas adjacent to china, *Chin. J.*
Oceanol. Limnol., 4, 1-16, 1986.
925
- Fang G., Kwok Y. K., Yu K., Zhu Y.: Numerical simulation of principal tidal constituents in
the South China Sea, Gulf of Tonkin and Gulf of Thailand, *Cont. Shelf Res.*, 19(7), 845-869,
1999.
- Fontes R. F. C. Castro B. M., Beardsley R. C.: Numerical study of circulation on the inner
930 Amazon Shelf, *Ocean Dyn.*, 58,187-198, 2008.
- Gabioux M., Vinzon S. B., Paiva A. M.: Tidal propagation over fluid mud layers on the
Amazon shelf, *Cont. Shelf Res.*, 25, 113-125, 2005.
- 935 Gonzalez-Pola C., Diaz del Rio G., Ruiz-Villareal M., Sanchez R.F., Mohn C.: Circulation



- patterns at Le Danois bank, an elongated shelf-adjacent seamount in the Bay of Biscay, Deep-Sea Res., Part I, 60, 7-21, doi: <http://dx.doi.org/10.1016/j.dsr.2011.10.001> , 2012.
- Guarnieri A., Pinardi N., Oddo P., Bortoluzzi G., Ravaioli M.: Impact of tides in a baroclinic
940 circulation model of the Adriatic Sea, J. Geophys. Res., 118(1), 166-183, doi:
<http://dx.doi.org/10.1029/2012JC007921>, 2013.
- Herzfeld M.: Improving stability of regional numerical ocean models, Ocean Dyn., 59(1), 21-
46, doi: <http://dx.doi.org/10.1007/s10236-008-0158-1>, 2009.
945
- Holt J., Hyder P., Ashworth M., Harle J., Hewitt H.T., Liu H., New A.L., Pickles S., Porter
A., Popova E., Allen J.I., Siddorn J., Wood R.: Prospects for improving the representation of
coastal and shelf seas in global ocean models, Geosci. Model Dev. 10, 499-523, doi:
<http://dx.doi.org/10.5194/gmd-2016-145>, 2017.
950
- Hu J. Y., Kawamura H., Hong H. S., Kobashi F., Xie Q.: Tidal features in the China Seas and
their adjacent areas derives from TOPEX/Poseidon altimeter data, Chin. J. Oceanol. Limnol.,
19, 293-305, 2001.
- 955 Kovalik Z., Luick J.: The Oceanography of Tides, Fairbanks, USA.
https://www.uaf.edu/files/sfos/Kovalik/tide_book.pdf , 2013.
- Le T. P. Q., Garnier J., Billen G., Théry S., Chau V. M.: The changing flow regime and
sediment load of the Red River, Viet Nam, J. Hydrol., 334, 199-214, 2007.
960
- Le Bars Y., Lyard F., Jeandel C., Dardengo L.: The AMANDES tidal model for the Amazon
estuary and shelf, Ocean Modell., 31, 132-149, doi : 10.1016/j.ocemod.2009.11.001, 2010.
- Le Hir P., Cayocca F., Waeles B.: Dynamics of sand and mud mixtures : A multiprocess-
965 based modelling strategy, Cont. Shelf Res., 31, 135-149,
doi :<https://doi.org/10.1016/j.csr.2010.12.009>, 2011.



Lefebvre J. P., Ouillon S., Vinh V. D., Arfi R., Panché J. Y., Mari X., Thuoc C. V., Torrétou
J. P.: Seasonal variability of cohesive sediment aggregation in the Bach Dang-Cam Estuary,
970 Haiphong (Vietnam), *Geo.-Mar. Lett.*, 32, 103-121, doi: 10.1007/s00367-011-0273-8, 2012.

Lyard F., Lefevre F., Letellier T., Francis O.: Modelling the global ocean tides: modern
insights from FES2004, *Ocean Dyn.*, 56(5-6), 394-415, doi:
<http://dx.doi.org/10.1007/s10236-006-0086-x>, 2006.

975

Ma F., Wang Y., Li Y., Ye C., Xu Z., Zhang F.: The application of geostatistics in grain size
trend analysis: a case study of eastern Beibu Gulf, *J. Geogr. Sci.*, 20(1), 77-90, 2010.

Madec G. Imbard M.: A global ocean mesh to overcome the North Pole singularity, *Climate
980 Dynamics*, 1, 381–388, 1996.

Manh D. V., Yanagi T.: A study on residual flow in the Gulf of Tonkin, *J. Oceanogr.*, 56, 59-
68, 2000.

985 Maraldi C., Chanut J., Levier B., Ayoub N., De Mey P., Reffray G., Lyard F., Cailleau S.,
Drevillon M., Fanjul E. A., Sotillo M. G., Marsaleix P. and the Mercator Research and
Development Team: NEMO on the shelf: assessment of the Iberia–Biscay–Ireland
configuration, *Ocean Sci.*, 9, 745–771, <http://dx.doi.org/10.5194/os-9-745-2013>, 2013.

990 Marsaleix P., Auclair F., Floor J. W., Herrmann M. J., Estournel C., Pairaud I., Ulses C.:
Energy conservation issues in sigma-coordinate free-surface ocean models, *Ocean Modell.*,
20(1), 61-89, <http://dx.doi.org/10.1016/j.ocemod.2007.07.005>, 2008.

Milliman J.D., Meade R.H.: World-wide delivery of river sediment to the oceans, *J. Geol.*,
995 91, 1-21, 1983.

Monahan D.: Mapping the floor of the entire world ocean: the general bathymetric chart of
the ocean, *J. of Oc. Technol.*, 3(1), 108, 2008.



- 1000 Natural Conditions and Environment of Vietnam Sea and Adjacent Area Atlas, Hanoi, 2007.
- Nguyen N. T.: Some peculiarities of the formation of tidal phenomena in the South China Sea. *Okeanologia*, 9, 235-249, 1969.
- 1005 Nguyen N. M., Marchesiello P., Lyard F., Ouillon S., Cambon G., Allain D., Dinh V. U.: Tidal characteristics of the gulf of Tonkin, *Cont. Shelf Res.*, 91, 37-56, <http://dx.doi.org/10.1016/j.csr.2014.08.003>, 2014.
- Nugroho D., Koch-Larrouy A., Gaspar P., Lyard F., Reffray G., Tranchant B.: Modelling explicit tides in the Indonesian seas: An important process for surface sea water properties, *Mar. Poll. Bull.*, 131, 7-18, <http://dx.doi.org/10.1016/j.marpolbul.2017.06.033>, 2018.
- 1010 Owens P. N., Batalla R. J., Collins A. J., Gomez B., Hicks D. M., Horowitz A. J., Kondolf G. M., Marden M., Page M. J., Peacock D. H., Petticrew E. L., Salomons W., Trustrum N. A.: Fine-grained sediment in river systems: environmental significance and management issues, *River Res. Appl.* 21(7), 693-717, 2005.
- 1015 Pairaud I. L., Lyard F., Auclair F., Letellier T., Marsaleix P.: Dynamics of the semi-diurnal and quarter-diurnal internal tides in the Bay of Biscay. Part 1 : barotropic tides, *Cont. Shelf Res.*, 28 (10-11), 1294-1315, <http://dx.doi.org/10.1016/j.csr.2008.03.004>, 2008.
- 1020 Penven P., Debreu L., Marchesiello P., McWilliams J. C.: Evaluation and application of the ROMS 1-way embedding procedure to the central california upwelling system, *Ocean Model.*, 12, 157-187, doi: 10.1016/j.ocemod.2005.05.002, 2006.
- 1025 Pritchard D. W.: A study of the salt balance in a coastal plain estuary, *J. Mar. Res.*, 13(1), 133-144, 1954.
- 1030 Pritchard D. W.: The dynamic structure of a coastal plain estuary. *J. Mar. Res.*, 15, 33- 42, 1956.



Tong Si Son: Mapping tidal flats in Vietnam using remote sensing techniques, PhD thesis, Univ. de Reims Champagne-Ardenne (in French), 2016.

1035 Smith W. H. F., Sandwell D. T.: Global seafloor topography from satellite altimetry and ship depth soundings, *Science*, 277, 1957-1962, 1997.

Soulsby R.L., Hamm L., Klopman G., Myrhaug D., Simons R.R., Thomas G.P.: Wave-current interaction within and outside the bottom boundary layer, *Coastal Engin.*, 21, 41-69, 1040 1993.

Stammer D. Ray R., Andersen O., Arbic B., Bosch W., Carrère L., Cheng Y., Chinn D., Dushaw B., Egbert G., Erofeeva S., Fok H., Green J., Griffiths S., King M., Lapin V., Lemoine F., Luthcke S., Lyard F., Morison J., Müller M., Padman L. Richman J., Shriver J., 1045 Shum C., Taguchi E., Yi Y.: Accuracy assessment of global barotropic ocean tide models, *Rev. Geophys.*, 52, 243-282. <http://de.doi.org/10.1002/2014RG000450>, 2014.

General Statistics Office: Statistical Yearbook of Vietnam 2017, Statistical Publishing House: Hanoi, Vietnam.
1050 http://www.gso.gov.vn/default_en.aspx?tabid=515&idmid=5&ItemID=18941 , 2017.

Toublanc F., Ayoub N. K., Lyard F., Marsaleix P., Allain D. J.: Tidal downscaling from the open ocean to the coast : a new approach applied to the Bay of Biscay, *Ocean Modell.*, 124, 16-32, <https://doi.org/10.1016/j.ocemod.2018.02.001>, 2018.

1055 van Maren D. S., Hoekstra P.: Seasonal variation of hydrodynamics and sediment dynamics in a shallow subtropical estuary: the Ba Lat River, Vietnam, *Estuar. Coastal Shelf Sci.*, 60(3), 529-540, 2004.

1060 Vietnam maritime administration (Vinamarine). Approved planning for dredging in Hai Phong port. Available online: <http://vinamarine.gov.vn> (accessed on 15 July 2018).

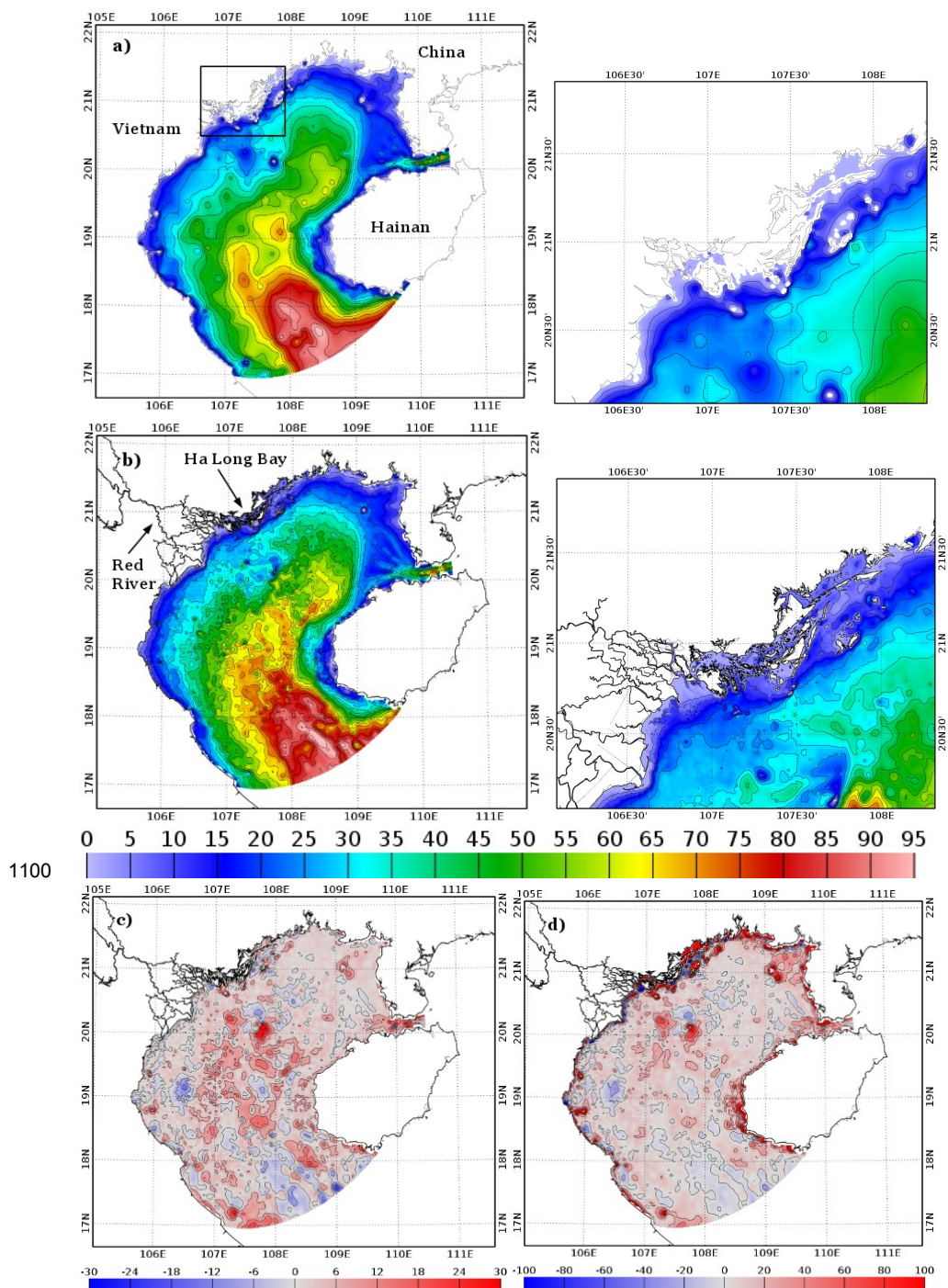
Vignudelli S., Cipollini P., Roblou L., Lyard F., Gasparini G. P., Manzella G., Astraldi M.:



- Improved altimetry in coastal systems : Case study of the Corsica Channel (Mediterranean
1065 Sea), *Geophys. Res. Lett.*, 32, 1-5, <https://doi.org/insu.bib.cnrs.fr/10.1029/2005GL022602>,
2005.
- Vinh V.D., Ouillon S., Tanh T.D., Chu L.V.: Impact of the Hoa Binh dam (Vietnam) on
water and sediment budgets in the Red River basin and delta, *Hydrol. Earth Syst. Sci.*, 18,
1070 3987–4005, doi:10.5194/hess-18-3987-2014, 2014.
- Vinh V.D., Ouillon S., Dinh V.U.: Estuarine Turbidity Maxima and Variations of Aggregate
Parameters in the Cam-Nam Trieu Estuary, North Vietnam, in Early Wet Season, *Waters*, 68,
1-33, doi: 10.3390/w10010068, 2018.
1075
- Wang X., Chao Y., Zhang H., Farrara J., Li Z., Jin X., Park K., Colas F., McWilliams J.C.,
Paternostro C., Shum C.K., Yi Y., Schoch C., Olsson P.: Modeling tides and their influence
on the circulation in Prince Williams Sound, Alaska, *Cont. Shelf Res.*, 63, S126-S137,
<http://dx.doi.org/10.1016/j.csr.2012.08.016>, 2013.
1080
- Wessel P., Smith W. H. F.: A global, self-consistent, hierarchical, high-resolution shoreline
database, *J. Geophys. Res.*, 101(B4), 8741–8743, doi:10.1029/96JB00104, 1996.
- Wetzel A., Szczygielski A., Unverricht D., Stattegger K.: Sedimentological and ichnological
1085 implacations of rapid Holocen flooding of a gently sloping mud-dominated incised valley –
an example from the Red River (Gulf of Tonkin), *Sedimentology*, 64, 1173-1202, doi:
10.1111/sed.12357, 2017.
- Wyrтки, K. : Physical oceanography of the Southeast Asian waters, 195 pp, Available from:
1090 <https://escholarship.org/uc/item/49n9x3t4>, 1961.
- Ye A.L., Robinson I. S.: Tidal dynamics in the South China Sea, *Geophys. J. Roy. Astronom.
Soc.*, 72, 691-707, 1983.
- 1095 Yu M.: A preliminary study of tidal characteristics in the South China Sea, *Acta. Oceanol.*



Sin., 6, 293-300, 1984.

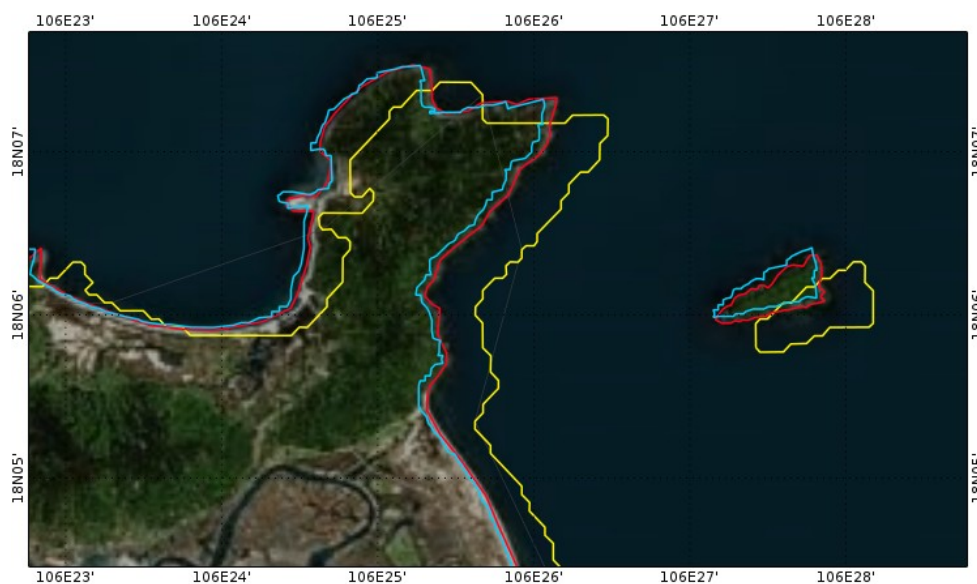


1100

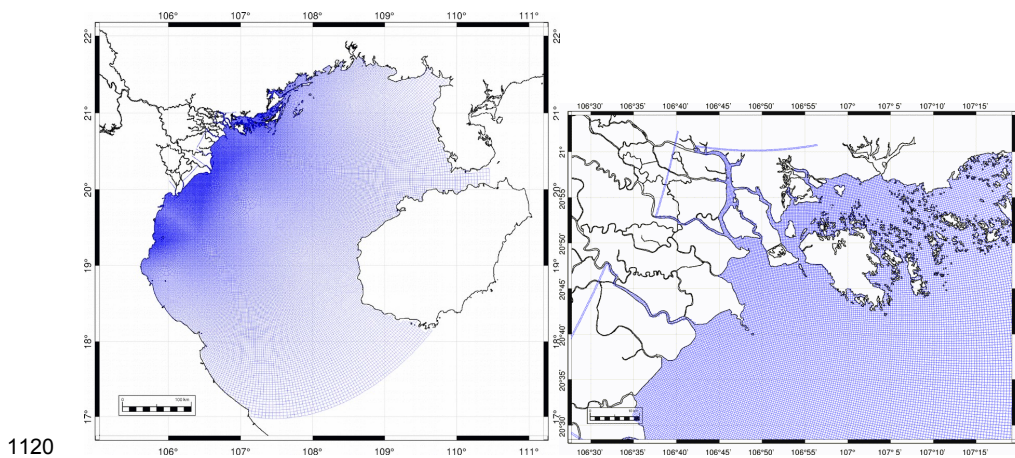


1105 **Figure 1: (a, left) Gebco bathymetry (in m) and (a, right) details of the Ha Long Bay area (black rectangle in a,left). (b, left) TONKIN_bathymetry data set merged with TONKIN_shorelines over GoT and (b,right) zoom in the Ha Long Bay area. (c) Absolute (m) and (d) relative (%) differences between TONKIN_bathymetry and Gebco bathymetry (in m).**

1110



1115 **Figure 2: Shorelines products from OpenStreetMap (blue line), GSHHS (yellow line) and TONKIN_shorelines (red line) superimposed on a satellite image downloaded from Bing over a small region of the GoT .**



1120

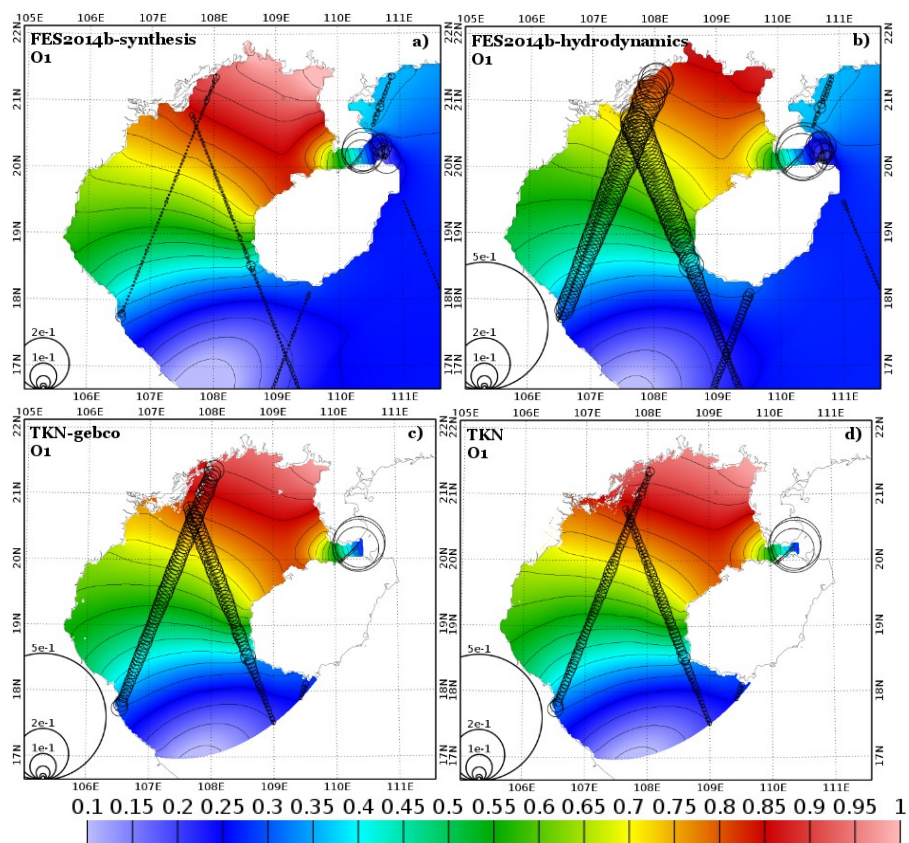
Figure 3: Model mesh over the GoT (left) with a zoom in Halong Bay region (right). The maximum refinement (150 m) is reached in the river channels.

1125

1130

1135

1140



1145

Figure 4: O1 tidal amplitude (in m) from different products: (a) FES2014b-synthesis, (b) FES2014b-hydrodynamics, (c) TKN-gebco and (d) TKN. The circle diameter is proportional to the complex error (Appendix ; Eq. 6) between the solutions and satellite altimetry (in m).

1150

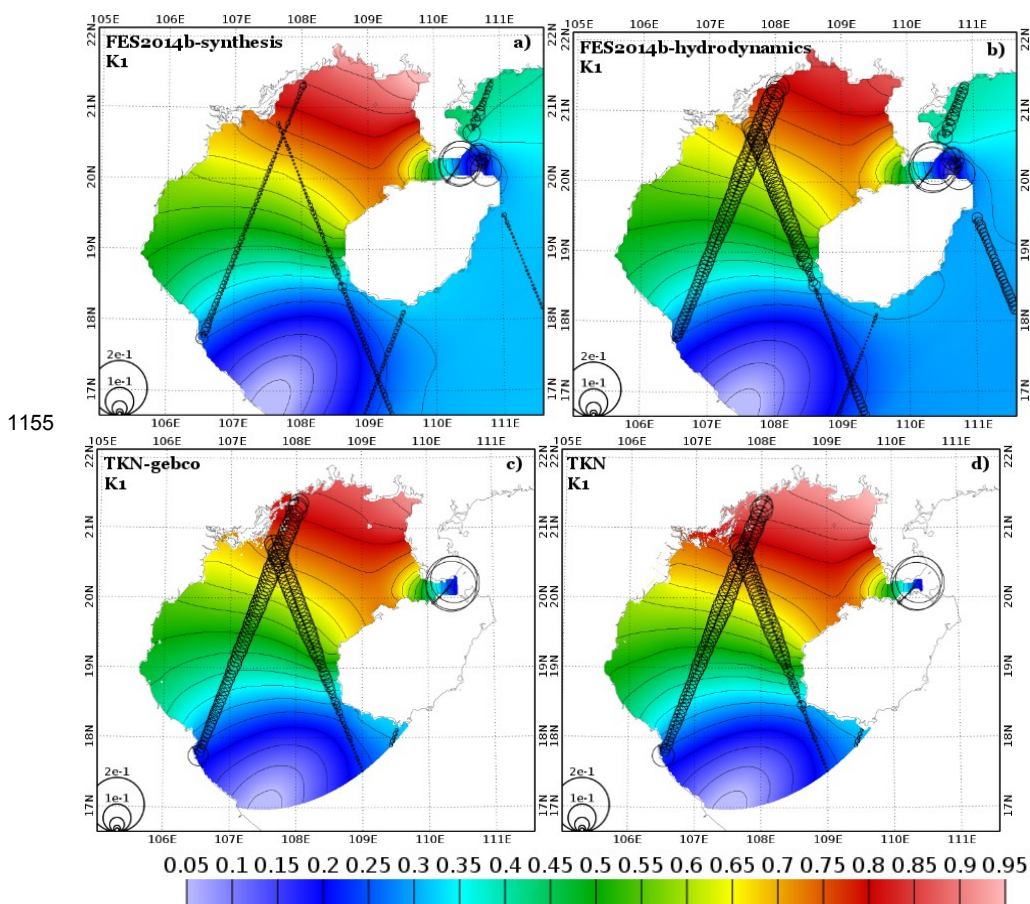


Figure 5: Same as Fig. 4 for K1.

1160

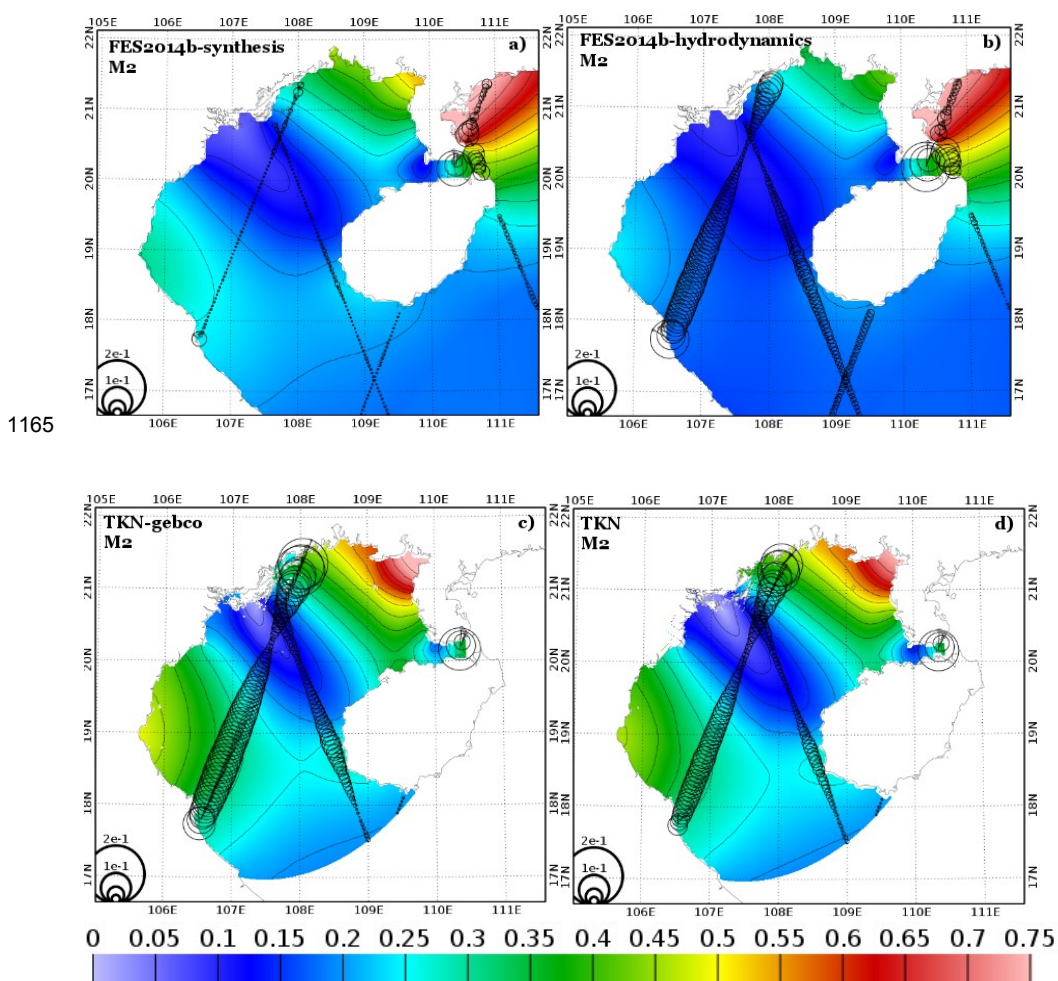


Figure 6: Same as Fig. 4 for M₂.

1170

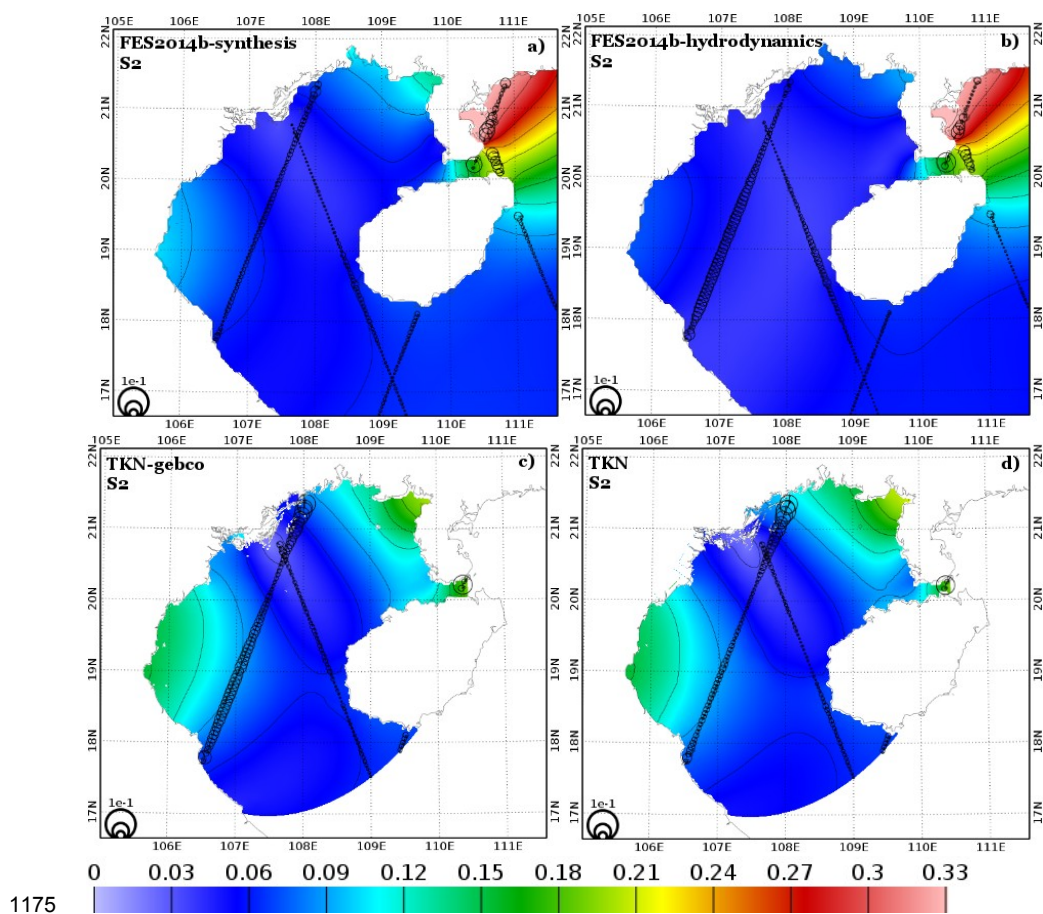
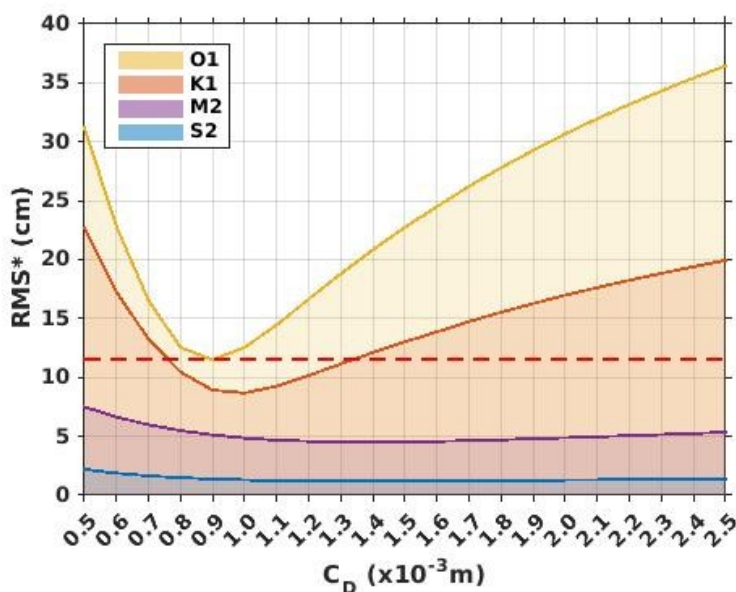


Figure 7: Same as Fig. 4 for S2.

1180

1185

1190



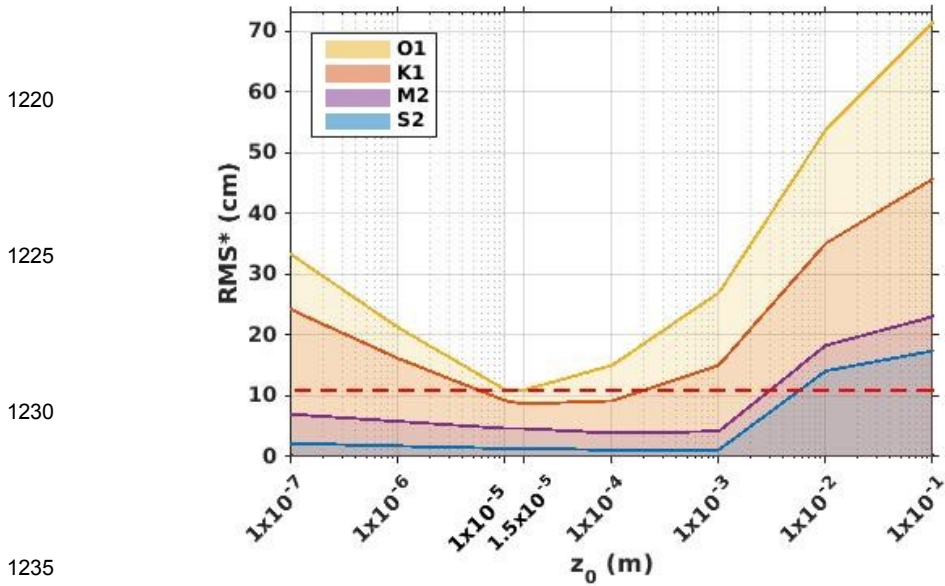
1195 **Figure 8:** Model complex errors (Appendix ; Eq. 6) relative to altimetry alongtrack data for tests performed with varying the values of the uniform drag coefficient C_D over the domain (SET1). The space in between two lines corresponds to the error for each wave. The yellow line therefore corresponds to the cumulative error for all four waves. The red dashed line corresponds to the smallest cumulative error, here equals to 11.50 cm, and obtained for $C_D = 0.9 \times 10^{-3} \text{ m}$.

1200

1205

1210

1215



1220

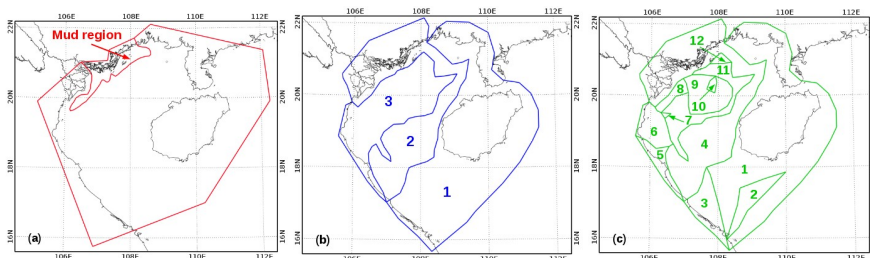
1225

1230

1235

Figure 9: Model complex errors (Appendix ; Eq. 6) relative to altimetry data for tests performed with varying the values of the uniform z_0 over the domain (SET2). The space in between two lines corresponds to the error for each wave. The yellow line corresponds to the cumulative errors for all four waves. The red dashed line corresponds to the smallest cumulative error, here equals to 10.96 cm, and obtained for $z_0=1.5 \times 10^{-5}$ m.

1240



1245

Figure 10: Spatial partitioning of the domain for the set of experiment SET3, (a), for SET4 (b) and for SET5 (c).

1250

1255

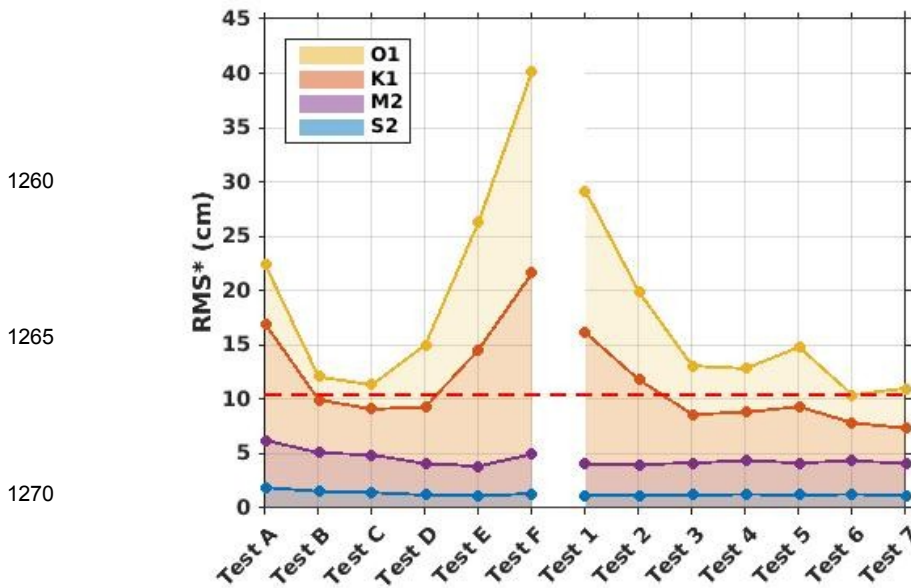


Figure 11: Model complex errors (Appendix; Eq. 6) relative to altimetry data for tests listed in Table 1 performed with non-uniform values of z_0 (SET3 and SET4). The space in between two lines corresponds to the errors for each wave. The yellow line corresponds to the cumulative errors for all four waves. The red dashed line corresponds to the smallest cumulative error, found for Test 6 (SET 4), equals to 10.43 cm.

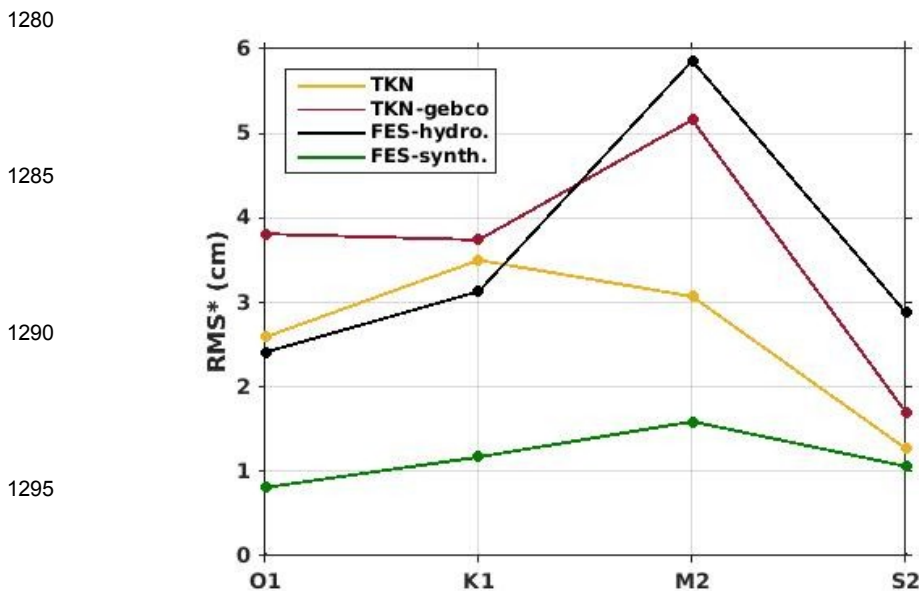


Figure 12: RMS* errors (Appendix ; Eq. 6) between numerical simulations (TKN, TKN-gebco, FES2014b-hydrodynamics and FES2014b-synthesis) and altimetry data for O1, K1, S2 and M2.



SET 3	A	B	C	D	E	F	SET 4	1	2	3	4	5	6	7
Mud region (r)	1.18 x10 ⁻⁴	1.18 x10 ⁻⁴	1.18 x10 ⁻⁴	1.18 x10 ⁻⁴	1.18 x10 ⁻⁴	1.18 x10 ⁻⁴	Region 1 (z₀)	1.0x 10 ⁻²	1.0x 10 ⁻³	1.0x 10 ⁻⁴	1.0x 10 ⁻⁴	1.0x 10 ⁻⁴	1.5x 10 ⁻⁵	1.5x 10 ⁻⁵
z₀ in the rest of the domain	1.0x 10 ⁻⁶	1.0x 10 ⁻⁵	1.5x 10 ⁻⁵	1.0x 10 ⁻⁴	1.0x 10 ⁻³	1.0x 10 ⁻²	Region 2 (z₀)	1.5x 10 ⁻⁵	1.5x 10 ⁻⁵	1.5x 10 ⁻⁵	1.5x 10 ⁻⁵	1.0x 10 ⁻⁴	1.5x 10 ⁻⁵	1.5x 10 ⁻⁵
							Region 3 (z₀)	1.0x 10 ⁻⁴	1.0x 10 ⁻⁴	1.0x 10 ⁻⁴	1.5x 10 ⁻⁵	1.5x 10 ⁻⁵	1.0x 10 ⁻⁴	1.0x 10 ⁻³

Table 1: Description of SET 1 and SET 2 (in m).

1305

Tides	O1		K1		M2		S2	
	Amplitude (cm)	Phase (°)	Amplitude (cm)	Phase (°)	Amplitude (cm)	Phase (°)	Amplitude (cm)	Phase (°)
TKN - this study <i>Compared to Satellite altimetry</i>	1.5	3.7	1.9	5.4	2.3	7.6	0.9	14.7
Minh et al. (2014) <i>Compared to Satellite altimetry</i>	2.4	8.4	2.8	10.4	8.0	7.8	2.4	17.7
Chen et al. (2009) <i>Compared to Gauge stations</i>	3.0	9.0	5.4	8.9	2.3	6.7	2.8	22.0

Table 2: Mean absolute differences (Appendix ; Eq. 7) of amplitudes (in cm) and phase (in deg) of M2, S2, O1, K1 constituents between our reference TKN and satellite altimetry. For comparison, the work of Minh et al. (2014) compared with satellite altimetry and the work Chen et al., (2009) compared to gauge stations are presented.

1310